

Optical Pumping

Nikitha Chalgeri
University of California Berkeley

(Dated: April 12, 2024)

In the presence of a weak static magnetic field, interactions between an atom's total magnetic moment and the local magnetic field induce uniform energy level splittings, a phenomenon known as the Zeeman effect, in which energy differences between neighboring magnetic substates (Zeeman states) are directly proportional to a precisely-defined frequency inherent to the atomic structure, denoted as the resonant frequency. To demonstrate and probe such an interaction, we utilize a vapor cell containing two alkali metal isotopes, ^{85}Rb and ^{87}Rb , and fluoresce circularly polarized Rubidium light to facilitate optical pumping, effectively generating a non equilibrium distribution in the extreme magnetic substates of the Zeeman regime. Such population change permits direct manipulation of magnetic substate transitions via application of incident resonant radiofrequency photons and is detectable by virtue of the opacity of the vapor cell to the optical pumping radiation. In this manner, we prepare the system for spectroscopic analysis and collect values of resonance at varied magnetic fields to derive critical properties of the Rubidium isotopes, specifically their intrinsic nuclear spins, as well as provide a measure of the magnitude and direction of the ambient magnetic field present in the laboratory. Our experimentation efforts yield nuclear spin values of $I_{85} = 2.54 \pm 0.003$ and $I_{87} = 1.53 \pm 0.0014$ for the ^{85}Rb and ^{87}Rb species respectively, closely aligning with their theoretically determined values of $I = 5/2$ and $I = 3/2$. We also implore various methods to estimate the ambient magnetic field in the vicinity of the experiment, leveraging the ultrasensitive magnetometry capabilities of the rubidium atomic vapor.

CONTENTS

I. Introduction	1	1. Intercepts from Linear Fits	16
II. Background and Theory	2	2. Zero DC Current	16
A. Atomic Structure	2	3. Positive & Negative Current	16
1. First Order Correction: Fine Structure	3	C. Zero Field Resonance	18
2. Second Order Correction: Hyperfine Structure	3	1. Transverse Optical Pumping	18
3. Third Order Correction: Weak Zeeman Effect	5	D. Nuclear Spins	19
B. Transitions	5	1. \vec{B} at the Bulb	20
C. Optical Pumping	6	E. Timescales for Optical Pumping	21
D. Optically Detected Magnetic Resonance	7	1. Exponential Fit	21
III. Experimental Setup	7	F. A Note on Error	22
A. Apparatus	7	V. Conclusion	22
1. Atomic Vapor Cell	7	VI. Appendix	22
2. Optical Pumping Optics	8	A. σ^+ Selection Rules	22
3. Radio-Frequency Coil	8	B. Breit-Rabi Derivation	23
4. Axial Magnetic Field	8	References	23
5. Overview	10	I. INTRODUCTION	
B. Procedure	11	Investigation of the optical spectra of atoms set the stage for establishing the complete quantum mechanical treatment of matter, revealing that the phenomenological qualities of an atom manifest themselves as well defined observables with a set of quantized, discrete values under the requisite that they are eigenstates of the system [1].	11
C. First Observation of ODMR	12	Naturally then, techniques rooted in atomic spectroscopy provide a powerful and direct mean to probe the internal structure of atoms. Such methods employ perturbing signals whose frequencies are exactly commensurate with the "Hertzian" resonances of the atom - or when scaled by the quantum of action, h , the energy difference, ΔE ,	12
D. Bulb Temperature	12		13
E. Lock-in Detection	12		14
F. Timescales for Optical Pumping	14		14
IV. Results & Analysis	14		14
A. Current versus Resonance Frequency	14		14
1. Weighted Least Squares Fitting	14		15
2. Unweighted Least Squares Fitting	15		15
3. Interpretation of Parameters and Fit	15		16
B. Ambient Field	16		

between two energy levels. Particularly, for an ensemble of atoms occupying some initial state configuration at a various point in time, such resonant signals tuned at proper frequency and polarization are capable of driving transitions between energy levels, thereby disclosing the precise value of the energy gap, ΔE . This information can subsequently be leveraged to deduce various properties of the atom and its constituents as well as aid in the understanding of the environmental conditions that directly influence ΔE .

Alkali atoms, such as the isotopes ^{85}Rb and ^{87}Rb , undergo a 3-tiered hierarchy of energy splittings due to their shell structures and field-free, subatomic interactions resulting in fine and hyperfine energy level stratification. The application of a weak magnetic field removes the degeneracy of the hyperfine levels as a result of the interaction between the field and the atomic magnetic moment, which is definitively specified by the vector sum of the total electronic and nuclear spin angular momenta. This process gives rise to Zeeman splittings, which, in the weak field regime, are substantially more granular and fine-scaled relative to the other energy level stratifications. In our experiment, we use optical pumping in conjunction with resonant radio frequency magnetic fields to first stochastically redistribute the population of atoms to the highest energy Zeeman state, then drive transitions between adjacent magnetic substates using a technique known as optically detected magnetic resonance (ODMR). The objective of this experiment is to characterize the Zeeman splitting of the hyperfine structural components in the ground state of the Rubidium atom under a known weak magnetic field. In the first phase of the experiment, we perform successive resonant radio frequency measurements at several magnetic field strengths to demonstrate the linear dependence of the atom's total magnetic dipole precessional frequency on the weak external magnetic field. This data then provides a straightforward method to derive the nuclear spins of both isotopes and the ambient magnetic field in the laboratory. In addition, we conduct time domain measurements to estimate the timescales of optical pumping (pumping time) and the steady state of rf-driven Zeeman transitions (relaxation time).

II. BACKGROUND AND THEORY

A. Atomic Structure

As a prologue to optical pumping, we first outline the atomic structure of Rubidium. We remark that the nuclear constituents of the Rubidium atom - the nuclei and the nucleons (protons and neutrons) - are well approximated as a point particle defined by an aggregated net charge, angular momentum, and magnetic dipole moment, and hence, we greatly reduce complexity by solely considering composite nuclear interactions with surrounding electrons and weak perturbing fields. Fur-

ther, the atomic number of Rubidium is 37, indicating that its electronic configuration contains only a single valence electron in the outermost shell ($5s$, with the coefficient 5 defining the principal quantum number of the largest orbital) with all other 36 electrons occupying the closed, inner shells. Evidently, the vast majority of electrons occupying the orbits of the Rubidium atom can be neglected since they are all fully paired and cannot mediate any interactions on the atomic or electronic scale, rendering their total angular momentum null. Upon closer examination, the rubidium atom is characterized by 3 distinct types of angular momentum - (i) the electronic orbital angular momentum, (ii) the intrinsic angular momentum arising from electronic spin, and (iii), the intrinsic angular momentum arising from nuclear spin - characterized by their respective quantum numbers L , S , and I . Moreover, due to the complete stability of the inner shells, the orbital angular momentum of the Rubidium atom is effectively defined by the occupation of the valence electron in the outer shell and thus, the electron's ground state, $5s$, and first excited state, $5p$, correspond to orbital angular momentum quantum numbers $L = 0$ and $L = 1$, respectively. Likewise, the electron spin for both the $5s$ ($L = 0$) and $5p$ ($L = 1$) states are fixed by the spin of the valence electron, $S = 1/2$. The intrinsic nuclear spins for each Rubidium isotope, ^{87}Rb and ^{85}Rb , are $I_{87} = 3/2$ and $I_{85} = 5/2$ [1]. With the relevant quantum numbers identified, we may now proceed to investigate subatomic interactions that culminate in the tripartite energy splittings of Rubidium under electrodynamic vacuum conditions. First and foremost, we note that every charged particle possessing angular momentum, whether it be orbital or spin, carries a magnetic moment associated with the operator of that respective momenta. Principally, magnetic interactions among these dipole moments are ultimately what induce perturbations altering the atomic system, which manifests as a spectrum of energy splittings with spacings, ΔE , that increase with the strength of the coupling energy. The largest energy splitting, and correspondingly the most dominant force, is attributed to Coulomb interactions between the nucleus and the valence electron characterized by the principal quantum numbers n and orbital angular momentum quantum numbers L . Abiding the framework of the central field approximation, the Hamiltonian defining this interaction simplifies to the familiar \hat{H} operator used in the single electron, hydrogen atom model [2].

The next order of lower-energy splittings arise from more delicate atomic and nuclear-scale interactions involving the intrinsic spins of the nucleus and electron. These interactions are treated as perturbative corrections in the subsequent sections. The complete energy level diagrams for isotopes ^{87}Rb and ^{85}Rb are depicted in Figure 1 and Figure 2, respectively.

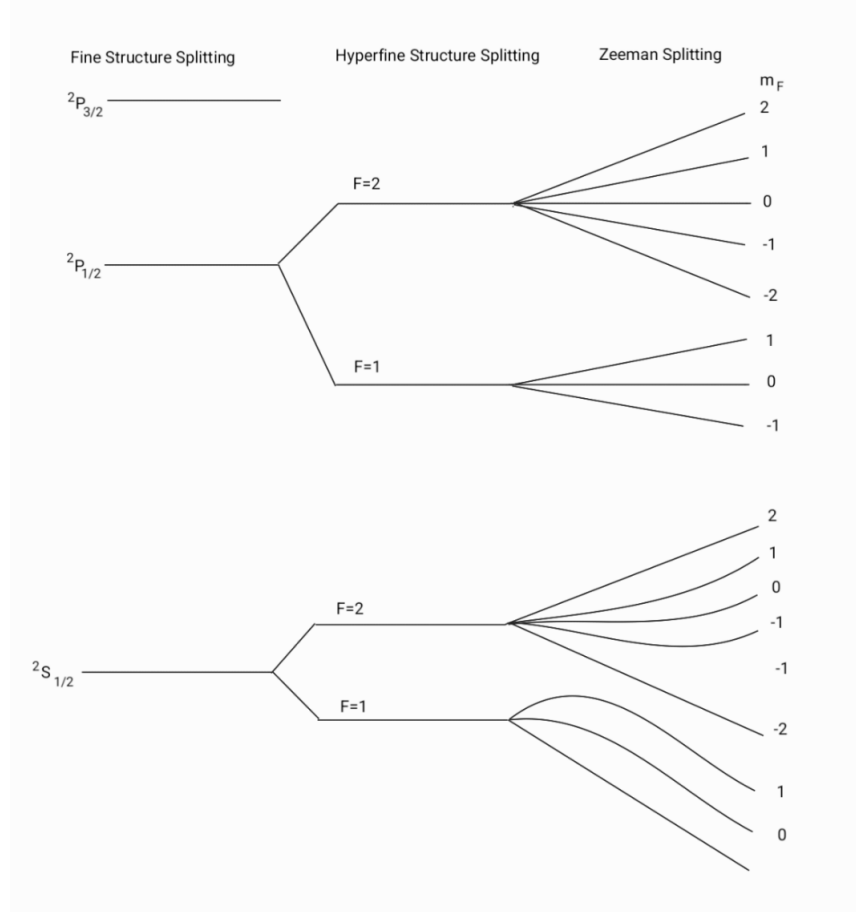


FIG. 1: Energy level diagram for ^{87}Rb .

1. First Order Correction: Fine Structure

Fine structure corrections spawn from relativistic effects in which an electron's orbit around a positively charged nucleus creates a magnetic field that couples with its spin magnetic moment. The interaction energy takes the form:

$$H_f = \vec{\mu}_L \cdot \vec{\mu}_S \propto \vec{L} \cdot \vec{S} \quad (1)$$

This interaction leads to the splitting of energy levels based on energy eigenstates characterized by definite total angular momentum $\vec{J} = \vec{L} + \vec{S}$ [1]. In particular, the different orientations in which the spin and orbital magnetic moments align correspond to different interaction energies [2]. Further, the quantization of these energies results in a discrete number of allowed configurations in which the magnetic moments can align, encapsulated by the total angular momentum, J , the characteristic good quantum number associated with the coupling basis that commutes with H_f . As a result, the set of all quantized values permissible for J (ranging from $L + S$ down to $|L - S|$ in integer steps) correspond to the number of possible orientations of electronic angular momenta and equivalently, the number of distinct splittings induced by

fine structure interactions. In the case of Rubidium, fine structure interactions stratifies the first excited state ($5p$) into sublevels corresponding to $J = 1/2$ and $J = 3/2$. In spectroscopic notation, these states are represented as, $^2\text{P}_{1/2}$ and $^2\text{P}_{3/2}$, where the superscript denotes the total electronic spin angular momentum ($2s + 1$), the letter "P" identifies the orbital angular momentum ($L = 1$), and the subscript designates the total angular momentum, J . The $5s$ ground state remains unperturbed to fine structure interactions since $L = 0$, and thus, the absence of orbital angular momentum leaves nothing for the electronic spin to couple with.

2. Second Order Correction: Hyperfine Structure

The existence of nuclear spin splits the fine structure levels further due to the electromagnetic interactions between the total electronic and nuclear magnetic dipole moments. The nuclear magnetic moment is defined:

$$\vec{\mu}_I = g_I \frac{e\hbar}{2m_p} \vec{I} \quad (2)$$

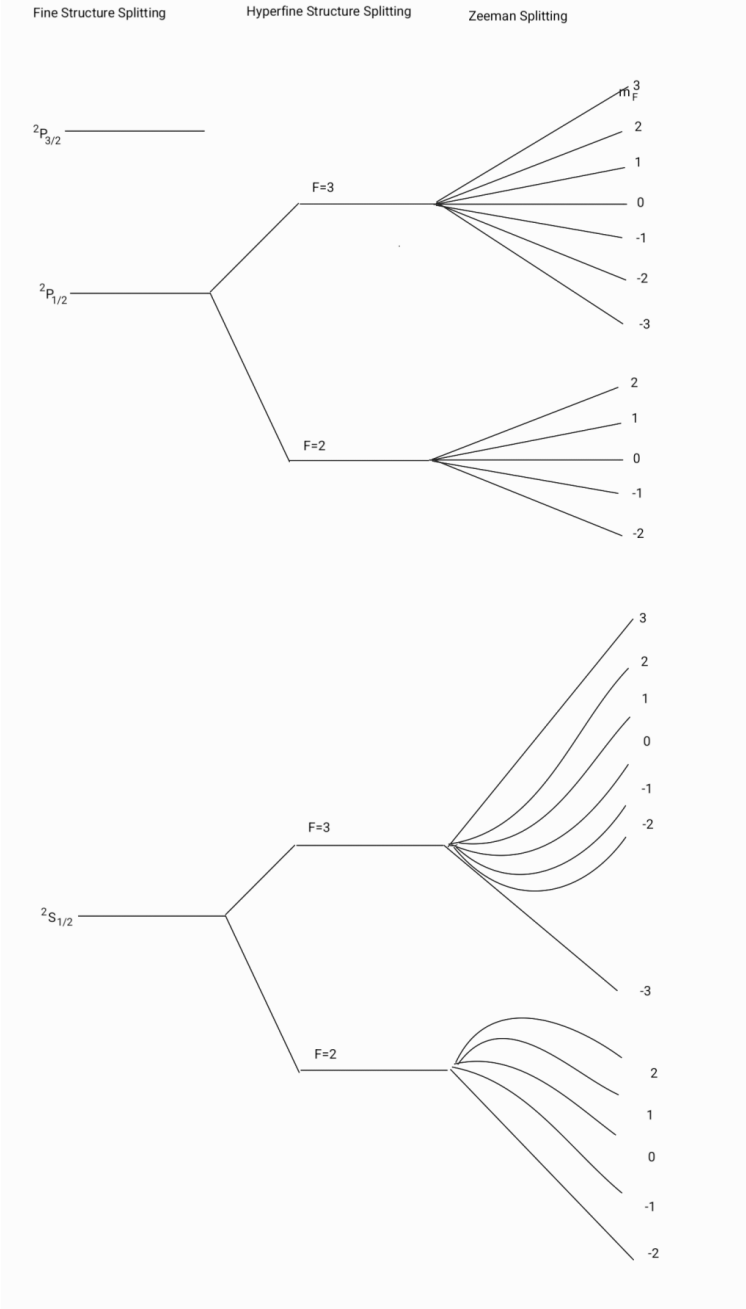


FIG. 2: Energy level diagram for ^{85}Rb

where g_I is the Lande g-factor corresponding to the nucleus and $\frac{e\hbar}{2m_p} = \mu_n$, the nuclear magneton. Upon closer examination, we note that energy differences between adjacent hyperfine sublevels are appreciably lower in energy relative to fine structure since the nuclear magnetic moment is inversely proportional to the mass of the proton (2000 times the mass of an electron), and as a consequence is significantly small in contrast to the magnetic moment of the electron, lending to a weaker coupling strength. The resulting perturbative interaction gives rise to hyperfine structure splittings with a characteristic en-

ergy defined by the following Hamiltonian operator:

$$\hat{H}_{hfs} = -\mu_I \cdot \mu_J \propto \vec{I} \cdot \vec{J} \quad (3)$$

Then, abiding by the rules of quantization and addition of angular momentum, the manifold of states each correspond to a definite total *atomic* angular momentum: $\vec{F} = \vec{I} + \vec{J}$. With the coupled basis, \vec{F} , the good quantum number becomes $F = J+I$, taking on possible values $J+I, J+1-1, \dots, |J-I|$. As a result, the excited electronic state splits into a number of hyperfine substates equal to $\min(2j+1, 2i+1)$. In consideration of the Ru-

bidium isotopes used in the experiment, $J = 1/2$ in the ground state, hence the number of hyperfine substates available for each isotope is 2. In particular, for ^{85}Rb , $F = \frac{5}{2} - \frac{1}{2} = 2$ and $F = \frac{5}{2} + \frac{1}{2} = 3$ and for ^{87}Rb , $F = \frac{3}{2} - \frac{1}{2} = 1$ and $F = \frac{3}{2} + \frac{1}{2} = 2$.

3. Third Order Correction: Weak Zeeman Effect

The interactions detailed above all manifest in a field-free environment, however in the presence of weak, perturbing magnetic field, even finer splittings can be generated. To see this, we first define a state space spanning the coupled basis of $\vec{F} = \vec{I} + \vec{J}$, in which we label states according to their total atomic angular momentum and its projection along the z axis F_z , whose magnetic quantum number m_F takes discrete, integer values in the range $\{-F, F\}$ [1]. In zero-field environments, m_F values associated with an isolated atomic system are degenerate. However, upon the introduction of an applied field, \vec{B} , the degeneracy is subsequently lifted, as the atom's magnetic moment begins to interact with the external field. The magnetic quantum number accordingly describes possible projections of the total angular momentum vector onto an external magnetic field axis (\hat{z} in our demonstration). The energy splittings that result from this interaction are referred to as Zeeman splittings. Consequently, the conglomerate Hamiltonian that encompasses both hyperfine and the weak, perturbing Zeeman interaction is expressed as:

$$H = H_{hfs} + H_Z = -\vec{\mu}_I \cdot (\vec{B}_J + \vec{B}_{ext}) - \mu_J \cdot \vec{B}_{ext} \quad (4)$$

where μ_J and μ_I are the magnetic dipole moments of the electrons and nucleus, respectively. As with the nuclear magnetic moment defined in Equation 2, we can similarly express,

$$\vec{\mu}_J = g_J \mu_B \vec{J} \quad (5)$$

as the total electronic magnetic moment, where $\mu_B = e\hbar/2m_e$ is the Bohr magneton and g_J is the Lande g-factor associated with the total electronic angular momentum, a variable proportionality constant that relates the electron's spin and orbital angular momenta together in order to yield a net magnetic moment [1]. Upon inspection, the Hamiltonian in Equation 4 can be compartmentalized into internal and external interactions: (i) the interactions between the nuclear and electronic magnetic moments are effectively captured by the term $\vec{\mu}_I \cdot \vec{B}_J = Ah\vec{I} \cdot \vec{J}$ and (ii) the perturbative effects arising from the external magnetic field on the energies of atomic magnetic dipoles are characterized by, $-(\vec{\mu}_I + \vec{\mu}_J) \vec{B}_{ext}$ [1]. Equation 4 can be analytically solved in the low-field limit for alkali-atom ground level, $J = 1/2$ and $F = I + 1/2$, to find the Breit-Rabi Equation: the resonance condition delineating the energy spacing between adjacent Zeeman states in which spacings vary linearly

with respect to the external field [1]. The total magnetic moment of an atom is defined to be the vector sum of the total electronic and nuclear magnetic moments, and thus, we use the Lande g-factor, g_F , to account for the relative contributions of the nuclear and electronic dipole moment to the total atomic magnetic moment:

$$g_F = g_J \frac{F(F+1) + J(J+1) - I(I+1)}{2F(F+1)} + g_I \frac{F(F+1) - J(J+1) + I(I+1)}{2F(F+1)} \quad (6)$$

Using g_F , we can convert the extrinsic portion of the Hamiltonian to reflect the interaction energy between the external field and the atom's total magnetic moment, $E = -g_F \mu_B \vec{F} \cdot \vec{B}$, in which case the solutions are in terms of the projection of the total angular momentum vector relative to the axis of \vec{B} :

$$E_z = -g_F \mu_B m_F \vec{B} \quad (7)$$

The energy spacings, ΔE , between Zeeman substates can then be expressed as [9],

$$\Delta E = |E_{m_F+1} - E_{m_F}| = g_F \mu_B \vec{B} \quad (8)$$

The region of interest for experimentation is the ground state, $^2S_{1/2}$, (as we will see in the next few sections), which is specified by quantum numbers: $F = I \pm 1/2$, $L = 0$, $S = 1/2$, and $J = 0 + 1/2 = 1/2$. If we insert these values into the Lande g-factor expression (Equation 6) and simplify, we derive:

$$g_F = \frac{2}{2I+1} \quad (9)$$

Hence, expressing $\Delta E = h\nu$ and noting that the ratio between the Bohr magneton and Planck's constant is $\frac{\mu_B}{\hbar} \sim 1.399$ MHz, we can derive the Breit Rabi in the low-field limit:

$$\frac{\nu}{\vec{B}_{ext}} = \frac{2.799}{(2I+1)} \frac{MHz}{G} \quad (10)$$

We refer the reader to the Appendix for complete treatment of the Breit-Rabi equation.

B. Transitions

The transitions involved in this experiment can be sectioned into two distinct types [3]. The first are electric dipole transitions between the $5s$ and $5p$ states derived from Coulomb interactions (D line transition). The energy of the first excited state are shifted by values of J such that the D line transition is split into two components: the D_1 line transition ($^2S_{1/2} \rightarrow ^2P_{1/2}$) and the D_2 line transition ($^2S_{1/2} \rightarrow ^2P_{3/2}$) [4]. The energy gap between the ground state and the first excited fine structure

states are sufficiently high enough to enter the optical radiation regime in which optical photons of the requisite resonant frequency can drive stimulated emission or absorption [3]. In the case of D_1 , the resonance condition is satisfied with incident photons of $\lambda \approx 795$ nm [4]. Alternatively, the D_2 line transition is activated with photons of wavelength $\lambda = 780$ nm [4]. Transitions within this optical regime must obey the following selection rules: (i) $\Delta L = \pm 1$, (ii) $\Delta F = 0, \pm 1$ (excluding transitions from states $F = 0 \rightarrow F = 0$), and (iii) $\Delta m_F = 0, \pm 1$. The second type of transitions have energy gaps with corresponding frequencies in the radiofrequency spectrum. Such magnetic dipole transitions drive population changes between magnetic substates in the Zeeman regime and are attendant to selection rules $\Delta m_F = \pm 1$ [3].

C. Optical Pumping

In the state of thermal equilibrium, the distribution of atoms in the vapor cell among energy states obeys laws of standard statistical mechanics. Particularly, for an isolated atomic ensemble, the Boltzmann factor provides an analytical means of gauging the relative probabilities of two energy levels being occupied [1]:

$$\frac{P_1}{P_2} = \exp\left(-\frac{E_2 - E_1}{k_B T}\right) \quad (11)$$

where k_B is the Boltzmann constant. It is evident that the distribution characteristically favors lower energetic configurations over higher ones, especially in the instance where the energy divisions are separated by an appreciable gap. To see this, consider the D_1 transition between the ground state, $^2S_{1/2}$, and the first electronic excited state, $^2P_{1/2}$ for ^{87}Rb (although the case follows in a very similar suit for ^{85}Rb). In this case, $\Delta E \approx 1.559\text{eV}$ and at room temperature, $k_B T \approx 0.026\text{eV}$ [4]. Hence, the Boltzmann factor is $\frac{P(^2P_{1/2})}{P(^2S_{1/2})} \approx e^{-60} \propto 10^{-27}$, implying a significant disparity between the fraction of atoms in first excited state versus the ground state. On the contrary, in thermodynamic equilibrium, the ratio of relative populations in the atomic vapor cell within the hyperfine levels ($F = I + 1/2$ and $F = I - 1/2$) and neighboring Zeeman states converge to unity, an indication of net zero spin polarization in the vapor, as expected with randomization of spin orientation in finite temperature conditions and absence of polarizing fields (to avoid redundancy, we omit the explicit calculation) [1]. The above analysis highlights the impact optical pumping has on our experimental system, in which a two-fold process coerces the atomic vapor cell out of the equilibrium state and grossly biases the relative population of atoms across the Zeeman and hyperfine levels in the ground state by means of optical irradiation [5].

To investigate the phenomena of optical pumping, consider a vapor cell of Rubidium atoms subject to a weak magnetic field inducing Zeeman splittings on the hyper-

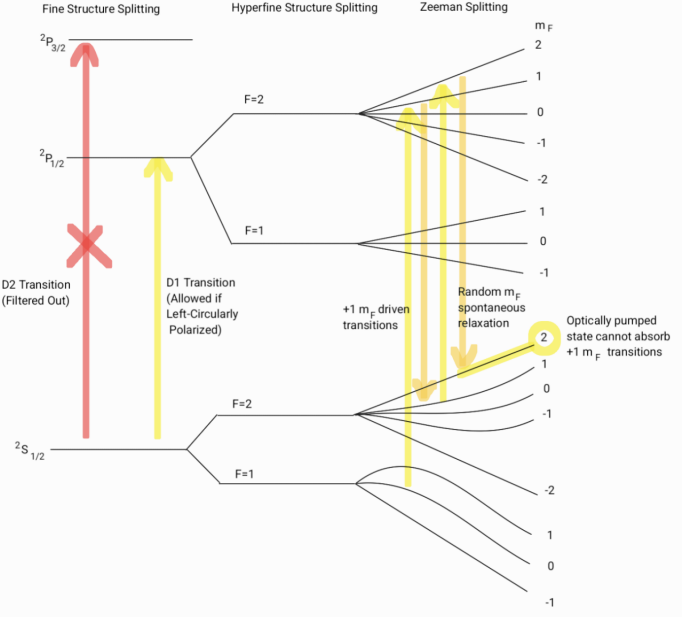


FIG. 3: Schematic illustration of an example trajectory of an ^{85}Rb atom as it experiences optical pumping by left circularly polarized light within a magnetic field \vec{B} , affecting the distribution of its magnetic substates.

fine level and exposure to an infrared light with resonance radiation capable of driving only D_1 line transitions ($^2S_{1/2} \rightarrow ^2P_{1/2}$), in which Doppler broadening of the radiation spans the range of hyperfine levels ($F = 2$ and 3 for ^{85}Rb or $F = 1$ and 2 for ^{87}Rb) [6]. Due to conservation of total angular momentum, if such radiation is left-circularly polarized (σ^+) so that angular momentum of the incident photons is aligned parallel to the axis of beam propagation (+ h), then upon absorption of a unit of D_1 radiation, the excited atom must gain one quanta of projected angular momentum for the case that the direction of incident beam propagation is parallel with respect to the external magnetic field vector [6]. Hence, only transitions attendant to the selection rule $\Delta m_F = +1$ are permitted. The resultant induced excited state is highly unstable, so in the reverse case ($^2P_{1/2} \rightarrow ^2S_{1/2}$) of rapid spontaneous emission of the incident photon, selection rules become slightly more variable, opening up equally probable transitions $\Delta m_F = 0, \pm 1$. Then upon reradiation, the probability of an atom populating a state with a greater value of m_F (a larger component of spin along the reference axis) is $2/3$ [6]. Ultimately, after many such cycles of absorption and emission, each atom in the ensemble is driven to the highest energy sublevel of the electronic ground state (or lowest depending on field polarity and anti parallel alignment of the direction of beam propagation and \vec{B}_{ext}), in which case, the atom loses its absorbing ability and can no longer excite to higher states if the D_2 line is filtered

such that no escape channels out of the pumped state exist. If the rate of population to the highest energy ground state is more rapid than the rate of depopulation via collisional or radiative relaxation, then the ground state with the highest magnetic moment becomes appreciably more occupied at the expense of other levels and we denote this state to be the "pumped state" [5]. An example of a possible trajectory of a ^{87}Rb atom pumped to its highest ground state, the $|F = 2, m_F = 2\rangle$ hyperfine sublevel, is depicted in Figure 3. In the case of the sister isotope, ^{85}Rb , the pumped state is the hyperfine sublevel, $|F = 3, m_F = 3\rangle$, of the ground state. From a heuristic standpoint, an optically pumped atomic system is detectable via higher intensity of the transmitted beam as in time, the vapor becomes increasingly more transparent to the circularly polarized D_1 resonance radiation [6]. In such a case, a photo detection system placed under the vapor cell receives more photons per unit area, and thus, we observe an output signal indicative of high light level [1].

D. Optically Detected Magnetic Resonance

After continuous application of resonant left circularly polarized light, we achieve maximum alignment of the atomic spin relative to the external magnetic field axis, in which all Rubidium atoms reside in their respective pumped states and no can longer absorb any incident photons (as described in Section *Optical Pumping*). Such a highly polarized state manifests as a strong DC current from a photodetector, which collects all transmitted light from the incident beam not absorbed by the atomic vapor cell. To induce magnetic dipole transitions between adjacent Zeeman substates, we bombard the system with radio frequency photons that are of the requisite resonant frequency to match the energy gap between Zeeman splittings. This subsequently prompts the atoms to rapidly oscillate between the magnetic substates such that a uniform distribution across the Zeeman states is generated, permitting continued absorption of optical irradiance despite the act of pumping. Essentially, the introduction of a resonant radiofrequency magnetic field coerces the atoms out of the pumped state, allowing the vapor to yet again absorb optical pumping σ^+ radiation, since a $\Delta m_F = +1$ is made available. The population shift culminates as a decrease in transmitted light intensity due to increased opacity in the vapor cell.

Therefore, impulses of a resonant radiofrequency photons imposed on the Rubidium atoms forms the crux of ODMR and provides a direct gauge of vapor magnetization via differential measurements of the vapor's opacity to incident pumping light [3]. Figure 4 demonstrates an instance of ODMR for the ^{87}Rb isotope.

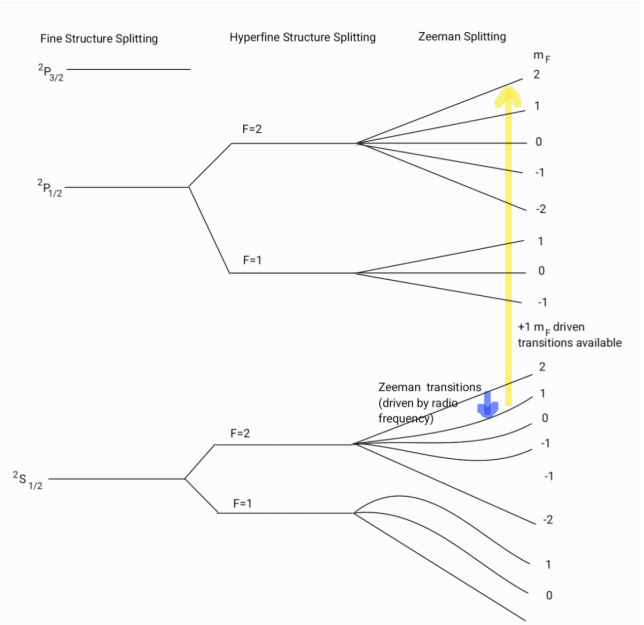


FIG. 4: Depiction of an induced Zeeman transition from a resonant radiofrequency photon and subsequent absorption of σ^+ light due an availability of a $\Delta m_F = +1$ transition (^{87}Rb isotope)

III. EXPERIMENTAL SETUP

For reference, a full diagram of the apparatus is displayed in Figure 5 and 6.

A. Apparatus

1. Atomic Vapor Cell

The essence of the experiment lies in the atomic vapor cell - a spherical glass bulb spanning a few inches in diameter encompassing the entire atomic system [1]. Within the heated absorption cell is a mixture of gas predominately comprising of a low-density neutral buffer gas with a small quantity of Rubidium. Without the presence of the buffer gas, the rate of disorienting collisions between the rubidium atoms and the cell walls would render optical pumping significantly less effective since the time for absorption and re-emission of electric dipole radiation is truncated by premature, frequent interactions with the bulb's walls [3]. The incorporation of buffer gas mitigates this issue because the ground state of the neutral buffer atoms is spherical symmetric, indicating that there are no Zeeman sublevels at the lowest energy level and as a consequence, the buffer gas cannot provide or absorb any unit of energy required for Zeeman transitions [3]. This implies that collisions between rubidium and buffer atoms conserve atomic spin, and as such, diffusion to the cell walls is delayed, permitting extended duration

of occupation in the pumped state and a greater pumping efficiency [1].

The concentration of rubidium atoms in the buffer atoms is directly influenced by the temperature of the bulb. At lower temperatures, a very small population of rubidium atoms adheres to the cell's walls such that the glass continues to appear transparent [1]. If the bulb temperature is increased, then a portion of the rubidium is discharged into the buffer gas [1]. Therefore, the density of rubidium within the optical bulb can be altered via adjustment's to the bulb temperature, which is accomplished through a resistive heating element administered by a Heater Control Unit (HCU). In order to find an optimal temperature range in which the volume of the optical bulb contains an adequate proportion of rubidium, we activate and modify the HCU. However, it is important to remark that the resistive heater generates an extraneous magnetic field that can disturb measurements for optically detected magnetic resonance and so, during measurement efforts, we opt to deactivate the heater.

2. Optical Pumping Optics

The apparatus utilizes a rubidium lamp subject to electronic discharge to generate the resonance radiation for optical pumping [1]. Photons emitted by the electronically excited rubidium precisely matches the absorption spectrum of the ground-state rubidium atoms in the vapor cell. Therefore, the emission spectrum of the lamp accounts all wavelengths corresponding to the D_1 and D_2 transitions for each of the rubidium species [1]. The emitted light from the lamp subsequently propagates through a pair of optical polarizers - the first filter selectively transmits circularly polarized light and the second is an interferometric filter (D_1 bandpass filter) designed to permit only light of corresponding wavelength 795 nm. A photodiode positioned directly under the rubidium lamp and vapor cell then collects the fluorescence of the transmitted beam after it propagates through and interacts with the atomic vapor, facilitating measurements of light intensity.

3. Radio-Frequency Coil

Surrounding the atomic vapor are two electromagnet coils aligned in series which are connected to an SRS DS345 synthesized function generator capable of producing highly resolvable waveforms. The function generator serves as a sinusoidal radiofrequency source (on the order of MHz) which induces a linearly polarized radio frequency magnetic field in a plane transverse with respect to the both the optical axis and the axis of the external Helmholtz coil field (introduced in the subsequent section). These electromagnet coils radiate radiofrequency photons resonant with the spacings between the mag-

netic substates, and thus have the capability to effectively drive transitions between the Zeeman sublevels of the ground state within the vapor.

Within the complete apparatus, the radiofrequency electromagnet coils, atomic vapor cell, optical pumping optics, and the heater all reside in a light proof, thermally insulated enclosure that mitigates ambient light interference with the weak optical signals [1].

4. Axial Magnetic Field

A magnetic field oriented parallel to the optical axis is imposed on the atomic vapor cell by a pair of coaxial, circular coils placed outside the light proof-box [1]. We regard these coils to be arranged in Helmholtz configuration, in which each of the N turns have identical diameters that exactly span the distance between the coils and carry the same current i . As a result, if we neglect thickness of the coil wire, a near homogeneous magnetic field is produced at the mid-plane:

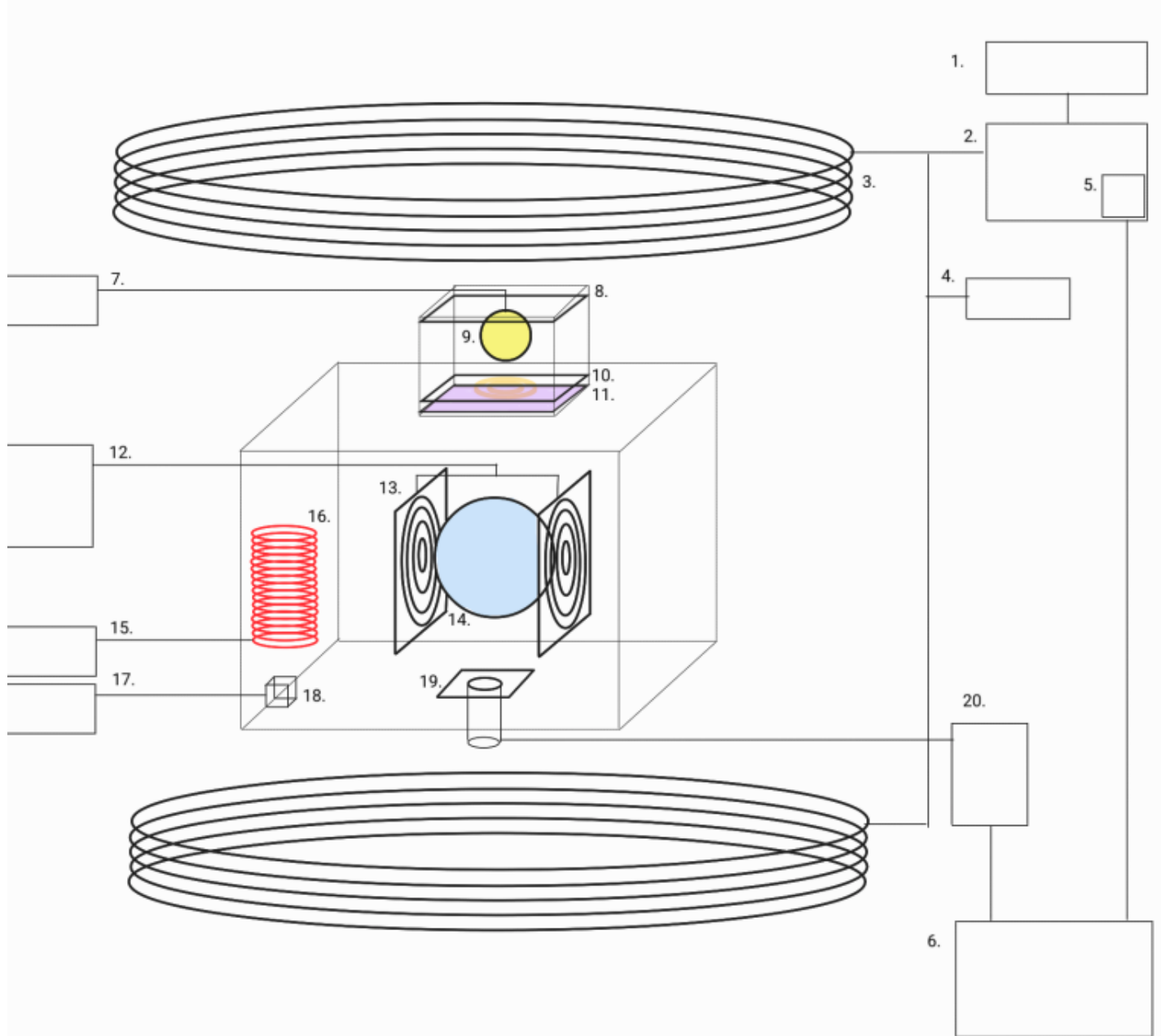
$$\vec{B}_{coil} = \frac{\mu_0 a^2 NI}{(a^2 + (a/2)^2)^{3/2}} = \frac{8\mu_0 NI}{5^{3/2}a} \quad (12)$$

where a is the radius of each coil, I is the current through the coils, and $\mu_0 = 4\pi \times 10^{-7} N \cdot A^{-2}$ is the magnetic permeability in vacuum. Simplifying further, we acquire the axial magnetic field in the Helmholtz condition,

$$\vec{B}_{coil} = (0.9 \times 10^{-2}) \frac{Ni}{a} \left[\frac{Gm}{A} \right] \quad (13)$$

Within our experimental setup, we assume the coils to have equal radii $a = 0.275\text{m}$ and $N = 135$ turns [1]. Although we treat the two coaxial coils in ideal Helmholtz condition, it is important to note that \vec{B}_{coil} can be subject to field inhomogeneity in which the magnetic field instead varies nonuniformly with respect to position. This poses as a systematic in our subsequent calculations and analysis in Section *Results*.

The coils are driven by a DC current combined with an overlaying 60Hz AC modulation. The DC component is generated by Agilent E3615A Power Supply and directly influences the Zeeman resonance frequency between the magnetic substates: the strength of the field applied on the atomic system increases in response to a stronger current drive, which as a result, widens the energy difference between adjacent Zeeman sublevels, effectively raising the the requisite resonance frequency needed to drive transitions. On the other hand, the AC component is derived from the standard 60Hz power mains, in which the signal's peak-to-peak voltage is damped by a variable transformer [1]. Hence, the composite magnetic field of the coaxial coils is essentially a DC current superimposed with a 60Hz AC current modulation. Further, the AC component plays a vital role for precise measurements of the Zeeman resonance frequency as detailed in Section *Lock In Detection*.



1. DC Power Supply
2. AC Modulation Unit
3. Helmholtz Coil
4. Current Meter (Shunt)
5. Phase Offset
6. Oscilloscope
7. Rubidium Lamp Power Supply
8. RF Oscillator and Reflector
9. Rubidium Lamp
10. Circular Polarizer

11. Band Pass Filter (D1 Transition)
12. DS345 Function Generator
13. Radio Frequency Coil
14. Rubidium 85 & 87 Sample
15. Heater Control Unit
16. Heater Coil
17. Volt-meter (Thermometer)
18. Thermal Probe
19. Photodiode
20. SRS SR560 Amplifier

FIG. 5: A complete diagram of the apparatus used for experimentation.

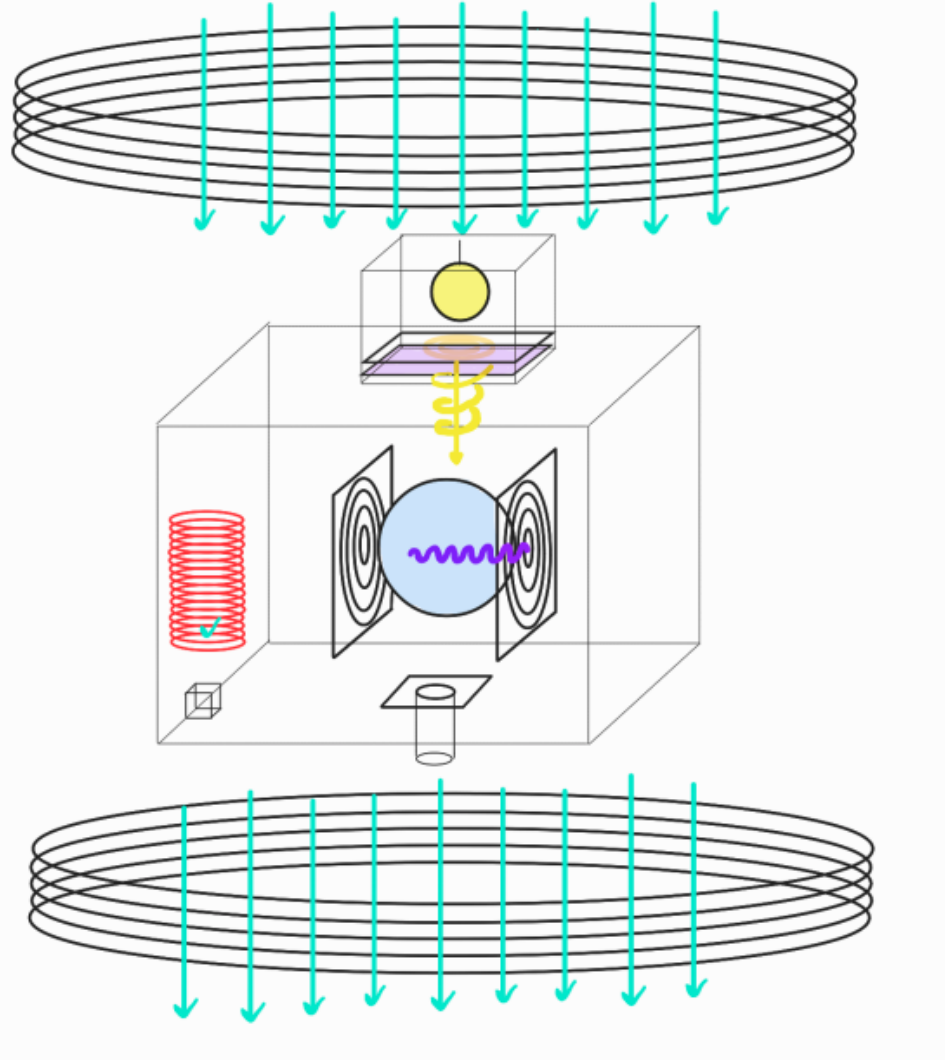


FIG. 6: A schematic illustrating various field line trajectories emerging from components of the apparatus. The two large, coaxial Helmholtz coils produce a near homogeneous magnetic field across the atomic vapor (blue lines). The Rubidium lamb directs incident photons through a D_1 bandpass filter and circular polarizer to generate optical pumping photons (yellow spiral). Finally, electromagnet coils positioned perpendicularly with respect to both the optical and Helmholtz axis produce rf photons that induce Zeeman transitions (purple wave)

5. Overview

Having introduced the components in our apparatus, we can now outline a brief overview of the procedure in order to conjoin the concepts described in Section *Background and Theory* and their physical realization via the components in our apparatus. First, the uniform magnetic field generated by the Helmholtz coils, combined by the background ambient field in the laboratory, lifts the degeneracy of the hyperfine levels, introducing Zeeman splittings. The subsequent two-step filtering process, as described in Section *Optical Pumping Optics* facilitates optical pumping, as it narrows the range of energy transitions to enable manifestation of the pumped state. The initial stage of circular polarization

ensures that all transmitted photons post filtering have a component of angular momentum in the direction of the beam equal to \hbar , and as such, upon interaction with the vapor cell, restricts excitable transitions to only those abiding $\Delta m_F = +1$, as required for conservation of angular momentum. The second stage of filtration (interferometric bandpass filter) restricts the excitation spectrum to only $^2S_{1/2} \rightarrow ^2P_{1/2}$ transitions, since it exclusively permits photons of 795 nm wavelength (characteristic of the D_1 transition), excluding the D_2 transition line and blocking an escape channel into the $^2P_{3/2}$ fine structure level. Post-modification of the incident beam, we achieve a state in which the rubidium atoms possess maximum projection of angular momentum along the optical axis, thereby completing a cycle of optical pumping.

The photo diode reads the high transmission of light and converts it into a current signal, which is subsequently amplified by the SRS SR560 amplifier and captured and analyzed on an oscilloscope. Next, a radiofrequency field generated by the electromagnet coils oriented orthogonal to the Helmholtz field and the optical axis of the electric dipole radiation at D_1 wavelength introduces radio frequency photons with frequency commensurate with the energy spacings between Zeeman sublevels, thus triggering transitions among these states if calibrated carefully. The photodiode captures this activity as an increase of opacity within the vapor cell, signifying a successful execution of the ODMR technique.

B. Procedure

C. First Observation of ODMR

In the following section, we detect Zeeman resonance features of the two Rubidium isotopes by maintaining a constant DC magnetic field across the vapor cell while gradually varying the radiofrequency across a wide spectrum. We closely monitor the photodiode signal for resonance events, identified as an abrupt change in the current signal output from the photodetection system. In this case, a sudden shift from a constant level of high light transmittance is indicative of increased opacity within the vapor cell, signaling the event in which the resonant rf field temporarily depumps atoms away from the pumped state and permits reabsorption of pumping photons to return back to the initial constant light level. Prior to measurement, we first increase the temperature of the cell to approximately 50°C in order to ensure a sufficiently dense rubidium atom population within the atomic vapor. As a first trial, we set an initial constant DC current of 1A through the Helmholtz coil. Despite setting the power supply to precisely 1A, we notice that the current meter displayed a reading of 1.014A, corresponding to a DC voltage of 10.14 mV across the shunt resistor (10 mV per ampere of current), however this value practically falls into the $\approx 1\%$ error margins of the current meter, so we consider the subsequent analysis evaluated at 1 ampere. To establish appropriate parameters for the radiofrequency sweep, we first calculate the expected resonance frequencies for each isotope using the Helmholtz formula (Equation 13) to determine the magnetic field in between the coils with an applied current of 1A then inputting the estimated field value into the Breit-Rabi equation:

$$\nu = \frac{2.799}{2I+1} (0.9 \times 10^{-2} \frac{Ni}{a}) MHz \quad (14)$$

Employing the coil parameters mentioned in section *Axial Magnetic Field* and characteristic nuclear spin values of $I = 5/2$ for ^{85}Rb and $I = 3/2$ for ^{87}Rb , we compute the following estimated resonance frequencies:

	Rubidium 85	Rubidium 87
ν (MHz)	2.06	3.09

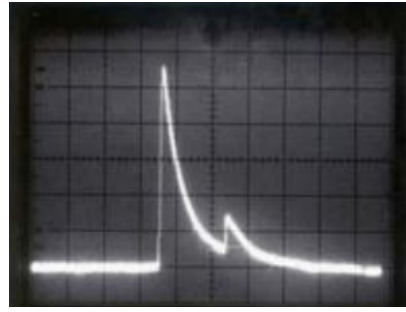


FIG. 7: An example of a characteristic resonance signature of the two isotopes. Estimated frequency values are derived by numerating the 1MHz large divisions to the left of the peaks then counting the finer scale divisions parameterized by the oscilloscope knobs.

With this approximation in hand, we configure the DS 345 function generator to produce a sinusoidal current linearly swept with a period of 100ms over a 3MHz range with the midpoint at around the resonance frequencies derived above and a 5V peak-to-peak output voltage. We then use the oscilloscope to capture and analyze the amplified photodiode signal against the rf magnetic field frequency and fix the axes such that the X-axis (Channel 1) reads the output swept by the SRS DS345 generator and the Y-axis (Channel 2) reads the amplified photodiode signal of the transmitted beam. Upon inspection, we observe resonances for both rubidium species at frequencies,

	Rubidium 85	Rubidium 87
ν (MHz)	2.202 ± 0.1	3.301 ± 0.1

The uncertainties affiliated with each value correspond to the midpoints of the finer scale markings on the oscilloscope, since the beam diameter on the scope had slight dispersion. We observe that the resonant signal of isotope ^{85}Rb has a higher relative amplitude than ^{87}Rb , indicating more intense light transmission. Under the assumption that light intensity is directly proportional to the number of atoms in the vapor cell, we can deduce ^{85}Rb is more abundant than ^{87}Rb , and therefore, the relative isotope abundances are staggered towards ^{85}Rb . As a brief assessment to variation of the resonance signal with respect to assorted parameters within our apparatus, we anticipate that:

- Increasing the sweep period set by the function generator varies the rf magnetic field over its fixed minimum and maximum values more rapidly. If the change in the field is too fast, then this may induce transitions in the non-adiabatic regime, in which the system can no longer quasi-statically evolve in response to the applied field, and as a consequence,

induce signal broadening. In such a circumstance of distortion, it is difficult to identify the sharpest point of the signal, corresponding to the resonance condition.

2. Increasing the rf peak-to-peak voltage would not impact the frequency at which resonance is observed, but rather increase the power of the incident resonant radio frequency field, applied onto the vapor cell.
3. A higher current in the rubidium lamp would increase the intensity of light available for optical pumping, since the density of incident pump photons, and by proxy, the transmitted beam, bombarding the vapor cell and collected by the photodiode is greater. As such, the photodiode would translate the higher fluorescence into a higher current signal and the signal strength on the scope would appear with greater amplitude.

D. Bulb Temperature

As mentioned in Section *Apparatus: Atomic Vapor Cell*, bulb temperature directly impacts the concentration of rubidium atoms in the vapor. Therefore, to quantitatively assess the optimal temperature that achieves maximum density of rubidium atoms, we observe variations in the ODMR signals extracted in the previous section with respect to thermal fluctuation. The temperature corresponding to the highest signal amplitude, indicating greatest population of rubidium atoms in the vapor, yields the most suitable temperature for experimental procedures. To extract this value, we heat the temperature of the light-proof box to roughly 50°C, and monitor the amplitude of the ODMR signal as the box slowly cools. At excessively high temperatures, we expect the diffusion of atoms to the glass wells to intensify because the thermal energy of the atoms dominates any efforts to subdue diffusion from interactions with the neutralizing buffer atoms. Thus, fewer rubidium atoms contribute to the optical pumping cycle, resulting in a lower degree of pumping efficiency and reduced signal amplitude. In a similar manner, at lower temperature, a significant proportion of rubidium atoms reside on the bulb's inner walls, hence, reducing the number of atoms available to populate the highest energy ground state during optical pumping and leading to a smaller amplitude signal. The results for this assessment are displayed in Figure 8

E. Lock-in Detection

The method for extracting resonant signals by holding coil current constant while varying the radiofrequency field, as described in Section *First Observation of ODMR*,

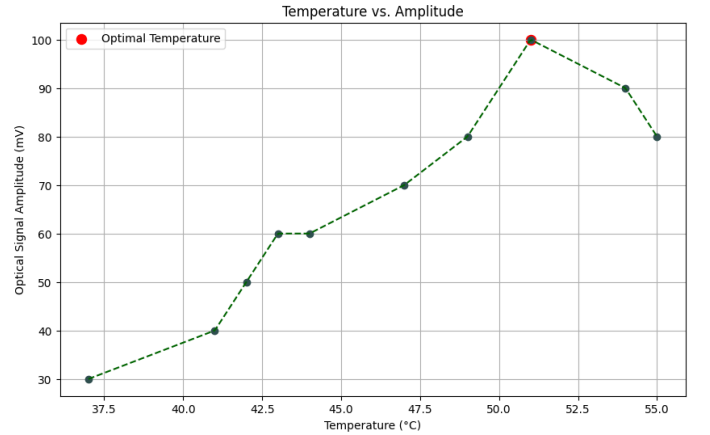


FIG. 8: Plot of signal amplitude vs. temperature in Celsius. We identified 51°C as the temperature corresponding to highest signal amplitude, indicated by the red dot.

is suboptimal - the process is inherently slow and moreover, the time it takes for the generator to sweep through individual points in the frequency range, captures a non negligible amount of low-frequency $1/f$ noise. As such, we adopt an alternative approach to identify the Zeeman resonances, in which we instead vary the current applied to the Helmholtz coils while maintaining a steady radiofrequency field.

To accomplish this, we parameterize the current sent through the coils in time by superimposing an AC component modulated at 60 Hz onto the DC component of the magnetic field. When projected onto the Zeeman resonant feature, modulation causes the magnetic field to oscillate orthogonally within a specific region of the signal geometry. Thus, in response, the photodiode's output oscillates temporally in consonance with the magnetic field modulation. We superpose the two perpendicular sinusoids on the oscilloscope, in which the time-dependent AC component of the magnetic field is plotted along the X-axis (Channel 1) and the synchronous oscillating photodiode output signal is plotted with respect to the Y-axis (Channel 2), generating the effective shape of a classic Lissajou curve, as depicted in Figure 9. Notably, in figure ??, we demonstrate that when the AC modulated magnetic field component carries a phase shift of $\pi/4$ and oscillates at twice the frequency of the sinusoidal photodiode signal, the points on the corresponding Lissajou directly map to points along the modulation of $\vec{B}_{coil}(t)$.

By varying the reference DC current about which the AC component modulates and observing synchronous variations in the photodiode signal, lock-in detection effectively enables differential measurements relative to current along the resonant signal. When the Lissajou figure showcases maximal symmetry, the reference DC component of the modulating magnetic field coincides with the point where the signal's gradient nears zero,

pinpointing the center of the resonance feature and by extension, the Zeeman resonance frequency. Conversely, off-resonance is explicit through an asymmetrical Lissajou figure, indicating that the incident magnetic field is offset from the minimum point of the signal.

To implement lock-in detection, we activate field modulation by flipping the Field switch on the Coil Driver panel and flipping the Phase Switch to turn on Phase Output. The signal from Phase Out traces the 60 Hz modulation applied to the Helmholtz coils. By assessing the degree of symmetry of the Lissajou curve, resonance frequency data for both isotopes are compiled over a range of DC current values from $([-3A, 3A]$ in 0.5A increments. In particular, in order to set initial conditions for measurement and distinguish resonant events corresponding to the two different isotopes, we begin by configuring the DC current value to 1A and use the values derived in the previous section to determine the order of resonant events, in which case, we anticipate the first occurrence of resonance (an appearance of Lissajou figure) to be characteristic to ^{85}Rb and the successive occurrence at the same current to belong to ^{87}Rb . Then, precise value of resonance frequency is determined by incrementally fine-tuning the rf frequency on the function generator until we deemed the Lissajou curve to appear most geometrically symmetric. This process was repeated for each subsequent value of current for both isotopes in our chosen range of $([-3A, 3A]$, which encapsulates both polarities of DC current across the Helmholtz coil as well the zero-crossing point, in which the resonance signatures observed are directly manifested by the surrounding ambient field in the laboratory since 0 DC current renders the magnetic field across the coils to be null.

In addition, we all also identify the point of zero-field resonance by completely deactivating the rf field and slowly adjusting current until the magnetic field across the Helmholtz coil balanced out the effective axial component of the ambient magnetic field, marked by the emergence of a Lissajou figure on the oscilloscope.

F. Timescales for Optical Pumping

In order to find the characteristic durations for optical pumping and subsequent relaxation we conduct a time-series analysis in which we configure the rf function generator to output a sinusoidal signal set at a constant resonance frequency corresponding to a specific current taken from the resonance vs current data. The sinusoidal signal amplitude is then modulated by a square wave set at a low frequency. With this rf field incident on the atomic vapor chamber, the amplified photodiode signal appears as a time-trace on the oscilloscope, with the scope triggered coincidentally with the square wave amplitude modulation. We recall that deactivation of the rf field should allow the atomic vapor chamber to reach the pumped state, such that the rubidium atoms achieve greatest magnetic polarization due to complete

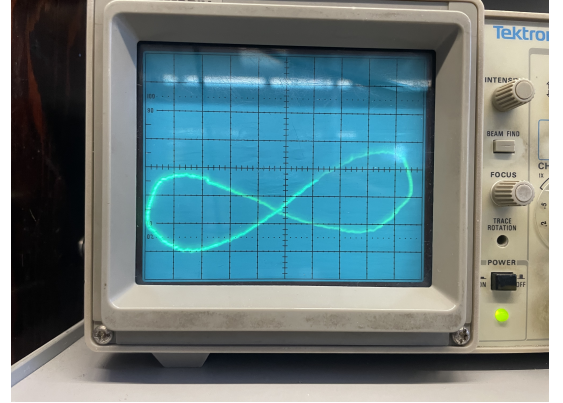
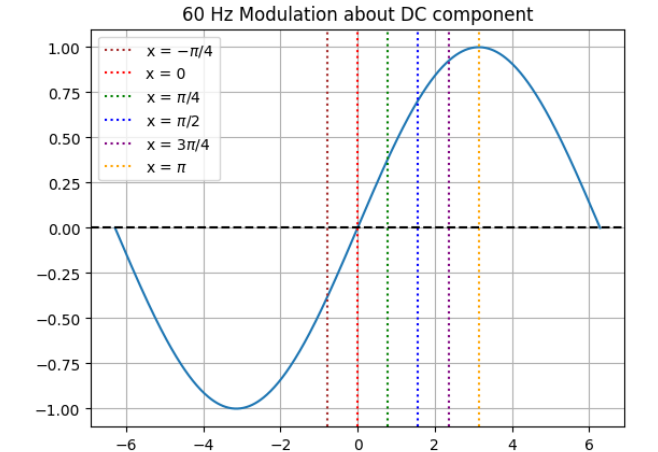
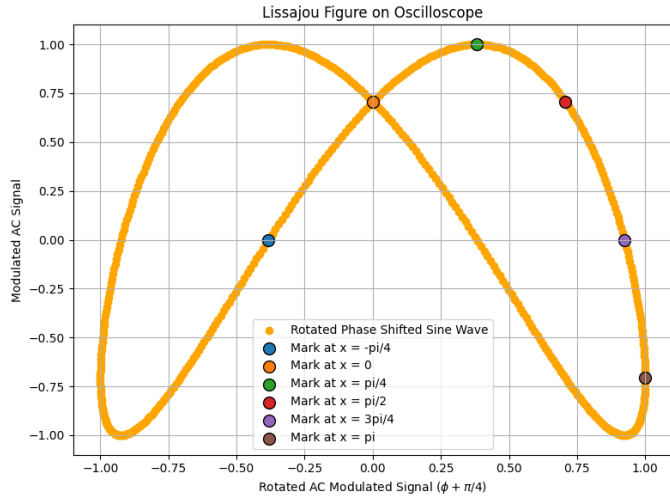


FIG. 9: Lissajou curve as observed on the oscilloscope. The X axis corresponds to the phase shifted AC modulated component of the coil's magnetic field whereas the Y-axis plots the out sinusoidal photodiode signal.

spin alignment and thus, can no longer absorb optically pumping photons, resulting in maximal transmittance of light through the vapor cell. Conversely, upon activation of the rf field, we expect the rubidium atoms to depolarize due to their atomic spins precessing away from the pumped state, resulting in gas becoming more opaque. The purpose of the square wave is to then turn the rf field on and off with a frequency sufficiently small as to permit the atomic vapor to reach a steady state between competing pumping and depolarizing rates. The resulting amplified trace on the oscilloscope then represents the change in light intensity as a function of time. We infer that the rising edge of the signal corresponds to pumping action, in which the time it takes for the signal to reach maximum amplitude is the characteristic pumping time. Likewise, the falling edge is indicative of the relaxation time, as the signal temporarily approaches a minimum. Additionally, we assume this minimum value, or the lowest transmitted light level, to correspond to the equilibrium state of the rf-driven vapor, such that the Zeeman sublevels are approximately equally populated. For measurement and analysis efforts, we set the sinusoidal signal at the resonance condition $\nu = 2.2025\text{MHz}$, corresponding to resonance frequency of the ^{85}Rb isotope at 1 ampere of current and the frequency of the square wave to 1 Hz. Zooming in on the oscilloscope trace, we are able to observe Rabi oscillations. Such a phenomena is manifested across a two level system, in the application of a sinusoidal temporal perturbation, like an influx of near resonant rf photons, causes the atoms to enter a coherent superposition in which the transition probability of finding the atom in, say either $m_F = 2$ or $m_F = 1$ oscillates in time. In essence, the oscillations are the atoms being periodically driven between two states by the external field.



((a)) 60Hz modulation about DC component (taken to be zero for the purposes of the visual demonstration).



((b)) A simulated Lissajou curve. The points along the 60Hz modulated signal directly map to the points on the figure when the AC component has a frequency twice that of the photodiode output and a phase shift of $\frac{\pi}{4}$ such that the waveform takes the functional form, $\sin(2t + (\phi + \frac{\pi}{4}))$

IV. RESULTS & ANALYSIS

A. Current versus Resonance Frequency

In the systematic approach elaborated in Section *First Observation of ODMR*, we measure the frequencies of radiofrequency photons resonant with the energy gap (ΔE) between magnetic substates while varying current applied to the Helmholtz coil. With these efforts, we aim to provide an explicit demonstration of the characteristic linearity in the low-field limit between the measured resonant frequency - and by direct proxy, ΔE - and the external magnetic field:

$$\hbar\nu = g_F\mu_B B \quad (15)$$

First, we note that whether the Zeeman transition induced by the radiofrequency drive adds or subtract from the atom's energy (depending on the external magnetic field alignment), linear polarization of the radiofrequency field always renders $|\Delta E| = h\nu$, thus readings on the radiofrequency function generator will solely provide information on the magnitude of energy gain, not the direction of energy change (i.e. whether the net energy of the atom has increased or decreased). Hence, on occasions in which field polarity of the Helmholtz coil is reversed, we correspondingly invert the sign of the measured frequency.

1. Weighted Least Squares Fitting

Subsequently, we employ ordinary least squares to construct an optimal linear fit to the resonance vs. current data. In this framework, the method identifies coefficients b_0 and b_1 in the linear functional form:

$$\hat{y} = b_1x + b_0 + \epsilon \quad (16)$$

such that the total sum of squares of the residuals is minimized (i.e. partial derivatives of the sum of squares formula with respect to the coefficients b_0 and b_1 is set to zero). Ordinary least squares makes the priori that the true model of the data is indeed of linear form associated with some degree of uncorrelated stochastic or systematic error, ϵ , whose default probability mass function is Gaussian. Using OLS, we first apply a weighted least squares fit to the resonance vs current data in which ϵ is transformed into covariance matrix with diagonal elements representative of weights to each data point, $w_i = 1/\sigma_i^2$. Within scope of the experiment, such uncertainty σ_i , specifically the upper and lower bounds of error, was empirically derived for each resonance frequency by searching for noticeable degrees of asymmetry in the Lissajou figure as the frequency of the radiofrequency magnetic field was adjusted around resonance in increments of $\sim 10 - 1000$ Hz. For a particular resonance, analysis of asymmetry produced unequal error margins in which the upper and lower frequency thresholds resulted in different deviations from the actual value. Therefore, to circumvent nonuniform uncertainty limits, we took the maximum difference between the frequency bounds and the derived resonance value, $\max(\nu_i^+ - \nu_i, \nu_i - \nu_i^-)$, to span the uncertainty range of a particular measured frequency ν_i .

We utilize two metrics to assess the quality of the weighted fit to the data: the Pearson chi-squared test (χ^2) and the coefficient of determination (R^2). The former is used to provide a statistical assessment of how well the data aligns with the null hypothesis that the underlying distribution is well represented by the linear functional form provided by ordinary least squares,

$$\chi^2 = \sum_i \frac{(O_i - N_{pi})^2}{\sigma_i^2} \quad (17)$$

in which O_i represents each observed resonance frequency at a specific DC current, N_{pi} is the predicted frequency lend by the null hypothesis (expected values derived from the OLS model), and σ_i is the uncertainty associated with datapoint O_i . Upon calculation, we derive $\chi^2 \approx 74.45$ and $\chi^2 \approx 71.32$ with 13 degrees of freedom (number of data points - number of parameters) with p-values, $p = 1 \times 10^{-10}$ and $p = 5 \times 10^{-10}$ for linear fits to the ^{85}Rb and ^{87}Rb respectively. Such a substantial χ^2 value with marginal p-values suggests that the proposed null hypothesis is either inadequate in representing the relation between current and resonance frequency or our empirical analysis of systematic error for each data point is highly insufficient in estimating the true error. Given the poor results provided by the χ^2 metric, we also employ the coefficient of determination, R^2 , as another gauge of goodness-of-fit for each of our fittings. R^2 measures the proportion of variance of our resonance frequencies that is explicable by the dependent variable in the OLS model and is expressed as the complement of the ratio between the sum of squares of residuals and the total sum of squares ($R^2 = 1 - \frac{RSS}{TSS}$). As such, we derive $R^2 = 1$ for both fittings, which contradictorily suggests that the model provides an essentially perfect fit to the data. Provided the discrepancies between R^2 and χ^2 for both isotope fittings, we infer that the estimated upper and lower bounds for each resonant frequency significantly underestimated the true systematic error in the measurement process, which consequently impacts the uncertainty for any successive analysis involving measured resonance frequencies. Values derived for the optimal linear fit and correlated properties of the atomic system are listed in Table I. The results of the weighted fitting on the resonance vs. current data with corresponding residual plots are shown in Figure 12.

	Rubidium 85	Rubidium 87	Property
b_1	2.0255 ± 0.002	3.0351 ± 0.002	$\frac{\nu}{i} \propto \frac{\nu}{B_T}$
b_0	0.1512 ± 0.002	$.2249 \pm 0.003$	ν_0

TABLE I: Optimal parameters derived for both isotope species using a weighted least squares fitting.

2. Unweighted Least Squares Fitting

The same analysis above is done for the case in which equal weights are assigned to each data point as opposed to biasing the covariance matrix generated for the best fit parameters with the systematic uncertainty derived from our measurement efforts. Rather, we quantify error by calculating the standard deviation of the residuals ($e_i = y_i - \hat{y}_i$), which are the differences between the actual data points and the computed values predicted by the linear fit. Again employing the chi-squared test (Equation 17), we obtain χ^2 values of 15 for 13 degrees of freedom, with a p-value of $\approx .32$ for both ^{85}Rb and ^{87}Rb .

Although the p-values fall into a lower range, the χ^2 from the unweighted fitting with error estimates drawn from deviation of the residuals indicates a significantly improved fit. The optimal parameters generated from the unweighted least square fittings are listed in Table II alongside the standard deviation of the residuals.

	Rubidium 85	Rubidium 87	$\sigma(e)$
b_1	2.025 ± 0.0017	3.0361 ± 0.002	0.011 ± 0.094
b_0	0.1521 ± 0.003	$.2259 \pm 0.004$	0.0132 ± 0.05

TABLE II: Optimal parameters derived for both isotope species using an unweighted least squares fitting. The errors on the residuals were derived from measured errors on ν .

Contrasting, we note that the optimal parameters from both the unweighted and weighted fittings are extremely similar, and thereby, we can conclude that the systematic uncertainty margins derived for resonance frequency values do not holistically encapsulate true error for each data point. This is justifiable given that the uncertainty bounds for resonance frequencies were determined using very narrow incremental step sizes (on the order of a few Hertz), and consequentially, are incapable of encapsulating the comprehensive biases inherent to the experiment that could interfere with measurement. As such, the weights, $1/\sigma_i$, could have disproportionately influenced the model, potentially obscuring the presence of other systematics tied to the data. With this in consideration, subsequent analysis dependent on measured values ν are likely affiliated with relatively underestimated propagated uncertainty. The plots for the unweighted fitting with corresponding residuals are displayed in Figure 13.

3. Interpretation of Parameters and Fit

Noting that the total external magnetic field inducing Zeeman splittings in the atomic structure is the field produced by the Helmholtz coil superimposed with the ambient magnetic field,

$$\vec{B}_{total} = \vec{B}_{coil} + \vec{B}_{ambient} \quad (18)$$

we interpret the y-intercepts of the plots for each isotope as their respective Zeeman resonance frequencies under the influence of solely $\vec{B}_{ambient}$. This is because zero current nullifies the magnetic field contribution from the coils. Furthermore, we infer that the intersection between the two best fit lines represents the point at which \vec{B}_{coil} and the axial component of the $\vec{B}_{ambient}$ exactly oppose one another, such that $\vec{B}_{total} \approx 0$ along the poles of the Helmholtz coil (see Figure 11). In addition, the slope of the best fit line provides an approximate ratio of the resonance frequency and the current which is directly

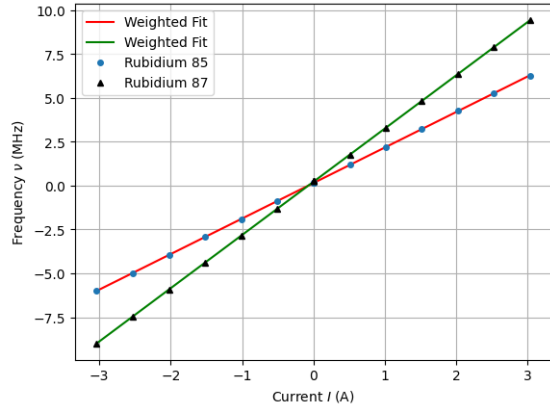


FIG. 11: Overlapped resonance vs. current plots for both isotopes. The intersection between the two lines represent cancellation of the magnetic field along the axial direction (optical/Helmholtz axis).

proportional to,

$$\frac{\nu}{\vec{B}_{ext}} = \frac{2.799}{2I+1} \frac{MHz}{G} \quad (19)$$

assuming that the total magnetic field (Equation 18) is in roughly linear correspondence with the DC current applied to the coils.

B. Ambient Field

In the following analysis, we introduce three approaches for quantifying the ambient magnetic field within vicinity of the experimental setup. As a point of reference, the Earth's magnetic field around UC Berkeley is approximately 0.477 Gauss.

1. Intercepts from Linear Fits

As discussed in section *Interpretations of Parameters and Fit*, the y-intercepts of the best-fit plots for each of the isotopes depicted in Figure 12 and Figure 13 provide estimates to the Zeeman resonance frequency induced by $\vec{B}_{ambient}$. At these particular points in the plots, the applied DC current is assumed to be zero. As evidently seen through the Helmholtz coil expression (Equation 13), the magnetic field through the coils is zero and the resonance frequency is presumably only dependent on the contribution from the ambient magnetic field. Rearranging Equation 19 provides,

$$\vec{B}_{ambient} = \frac{(2I+1)\nu_0}{2.799} [G] \quad (20)$$

where ν_0 represents the resonance frequency at 0 applied current. Therefore, using the y-intercepts provided by

the weighted least-squares fitting and Equation 20, we offer estimates for the ambient field for each isotope listed in Table III. Here, the errors are derived from the stochastic uncertainty for each optimal fit, which preliminarily incorporates the systematic errors deduced from the empirical approach outlined in Section *Weighted Least Squares Fitting* to construct a holistic covariance matrix.

	Rubidium 85	Rubidium 87
$B_{ambient}$	0.324 ± 0.005	0.321 ± 0.004

TABLE III: Ambient field values estimated using the y-intercepts of the resonance vs current plots.

2. Zero DC Current

The following method follows in a highly similar suit as the method outlined in the previous section. However, rather than using the optimal y-intercept provided by the weighted model fitting, we instead use a direct reading of the resonance frequency when the DC Current is physically set to 0 to define ν_0 in Equation 20. The calculated $\vec{B}_{ambient}$ values are listed in Table IV. In light of inadequate error margins derived for the numeric values of ν , we also incorporate the additional 1% error margins associated with the current meter readings in order to mitigate underestimation of uncertainty. If the true current is indeed slightly shifted from the reading provided by the current meter, then there could be a very small, stray field through the coils induced by a current within range $[-0.01, 0.01]$:

$$\Delta \vec{B}_{coil} = \frac{N\Delta i}{a} (0.9 \times 10^{-2}) \frac{Gm}{A} \quad (21)$$

Hence, assuming that the current meter error margins are independent from the systematic uncertainty associated with ν (which may not be the case), we add the errors in quadrature, $\sigma(\vec{B}_{ambient}) = \sqrt{(\frac{(2I+1)(\Delta\nu_0)}{2.799})^2 + (\Delta \vec{B}_{coil})^2}$ to derive error margins for the ambient field.

	Rubidium 85	Rubidium 87
$B_{ambient}$	0.371 ± 0.044	0.367 ± 0.044

TABLE IV: Ambient field values estimated using the resonance frequency value when the DC current supply is set to 0.

3. Positive & Negative Current

An alternative approach to estimating the ambient magnetic field relies on the assumption that currents of equal magnitude produce magnetic fields of identical

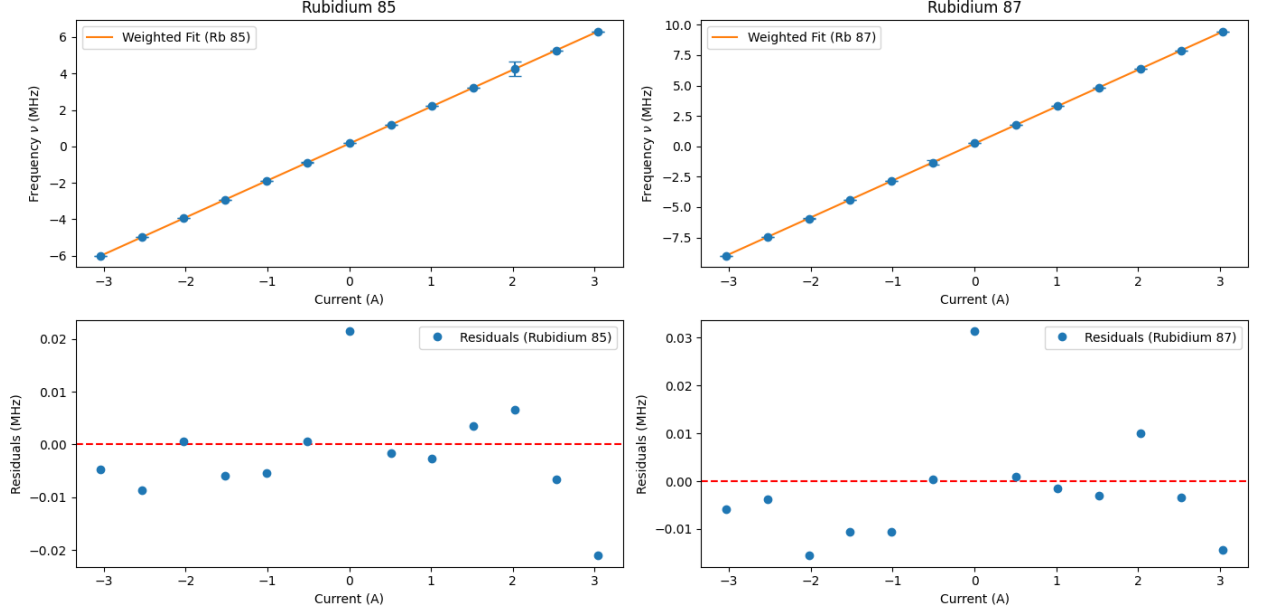


FIG. 12: Weighted least squares fitting applied to ^{85}Rb and ^{87}Rb with corresponding residual plots.

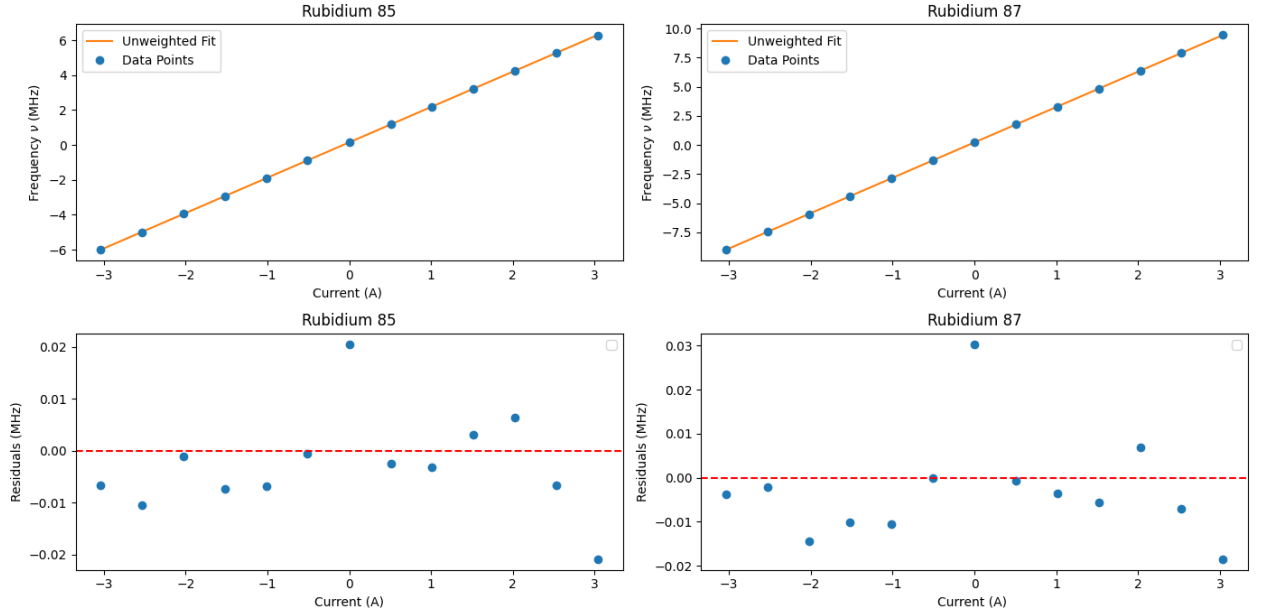


FIG. 13: Unweighted least squares fitting applied to ^{85}Rb and ^{87}Rb with corresponding residual plots.

strength. In other words, regardless of reversal of current polarity, the resulting magnetic field is equivalent for the same absolute value of current. Utilizing this premise, we use resonant frequencies at DC currents of 1.014A and -1.014A (as read by the current meter) to provide an appraisal of \vec{B}_{ambient} . Using the Breit-Rabi Equation (Equation 19), we obtain the following expressions for the resonance frequencies associated with positive and

negative currents respectively,

$$\nu^+ = \frac{2.799}{2I+1}(|\vec{B}_{\text{coil}}| + |\vec{B}_{\text{ambient}}|) \quad (22)$$

$$\nu^- = \frac{2.799}{2I+1}(|\vec{B}_{\text{coil}}| - |\vec{B}_{\text{ambient}}|) \quad (23)$$

Combining Equations 22 and 23 and rearranging to solve for $|\vec{B}_{\text{ambient}}|$, we arrive at,

$$|\vec{B}_{\text{ambient}}| = \frac{1}{2} \left(\frac{|\nu^+ - \nu^-|}{2.799} \right) (2I+1) \quad (24)$$

From this method, we are able to extract the quantities for $\vec{B}_{ambient}$ recorded in Table V. The derived errors are the propagated systematic uncertainties for ν^+ and ν^- ,

$$\sigma(\vec{B}_{ambient}) = \frac{1}{2} \frac{\sqrt{(\Delta\nu^+)^2 + (\Delta\nu^-)^2}}{2.799} (2I + 1) \quad (25)$$

	Rubidium 85	Rubidium 87
$B_{ambient}$	0.320 ± 0.01	0.319 ± 0.007

TABLE V: Ambient field values estimated using the same absolute value of current.

Although the three methods discussed above all provide ambient field strengths in similar ranges, they all are in disagreement with the magnetic field directly attributed to the Earth's core at our latitudinal and longitudinal range (0.477 G). Such deviation is explicable by considering the environmental fluctuations in our surroundings in which currents in power lines, the rebar in the walls, and magnetic materials inside the laboratory all pose as interference to the total ambient field subject to the atomic vapor cell [1]. Moreover, citing the conclusion of the analysis in Section *Weighted Least Squares Fitting*, we note that the error margins derived for each ambient field value are likely a severe underestimate of the actual systematic error since they rely on the unfit uncertainty bounds extracted for the resonance frequency values (especially Method 1). Although we attempt to partially circumvent this with the integration of the uncertainty associated with the shunt resistor, it is likely not sufficient to represent true error bounds. For instance, inhomogeneities in the magnetic field between the coils represent another source of potential systematic error, in which case our experimental setup does not fully abide by ideal Helmholtz configuration. Consequently, any calculations that rely on the Helmholtz coil equation (Equation 13) may be subject to greater uncertainty, and thus affecting the precision and accuracy of our measurements and reliability of our derived error margins.

C. Zero Field Resonance

With the radiofrequency modulation turned off and current steadily varied, a zero field resonance condition is detected when the magnetic field generated by the coils neutralizes the axial ambient magnetic field, such that $\vec{B}_{total} \approx 0$ along the optical axis. Such an event was identified at DC current:

$$I = -0.07737 \pm 0.071A \quad (26)$$

where the error margins were derived by assessing the contribution of two systematic errors - variation in the symmetry of the Lissajou figure as current is incrementally shifted as well as the 1% error margins from the

current meter. Under the assumption that these systematic errors are completely independent, we use quadrature error propagation to calculate uncertainty bounds (for simplicity, 1% error margins were neglected for the observed upper and lower current bounds). As such, we examine another way to estimate the ambient field. Using Equation 20 and considering that in the given scenario $\vec{B}_{coil} \approx -\vec{B}_{ambient}$, we deduce that the amount of field strength required by the coils to balance out the axial component of the ambient field is,

$$\vec{B}_{coil} = -0.342 \pm 0.312G \quad (27)$$

in which the error affiliated is simply the current error scaled by the constant factor in the Helmholtz equation. Hence, $\vec{B}_{ambient}$ is simply the inverse of Equation 27.

1. Transverse Optical Pumping

If the magnetic field produced by the Helmholtz coils is not perfectly aligned with the ambient magnetic field, then the detected zero field resonance may be a direct consequence of the residual ambient magnetic field in the transverse plane with respect to the optical axis, which remains unaffected by the opposing Helmholtz field. To understand why such a mechanism induces a resonance feature, we first treat the interaction between the atomic magnetic moment and the external magnetic field in a rotational frame then outline a brief exploration of transverse optical pumping on our experimental setup.

Recall that an isolated atom is akin to a gyromagnet in which an angular momentum and magnetic moment emerges as a result of its atomic spin [7]. The presence of a weak local magnetic field exerts a torque on the magnetic moments of the rigid atomic system,

$$\vec{\tau} = \vec{\mu} \times \vec{B}_{ext} \quad (28)$$

prompting the atom's magnetic moment vector to experience conical precession about the axis of the static magnetic field at the characteristic frequency of the ground state [7]. The rate of precession is denoted as the Larmor frequency (ω_L) and is precisely analogous to the resonant frequency previously discussed, but treated in a radial coordinate system to model angular dynamics,

$$\omega_L = \gamma \vec{B}_{ext} \quad (29)$$

where γ is the gyromagnetic ratio, a proportionality constant equal to $\frac{\mu_B g_F}{\hbar}$. With this in consideration, we can now address the scenario in which the atomic vapor cell in our experiment is subject to transverse optical pumping, in which the applied field is in a direction perpendicular to the optical pumping light. Generally speaking, the expected value of the transverse magnetization of the vapor, $\langle \vec{M}_T \rangle$, is zero for the case that the incident optical pumping radiation is in a well-defined state of polarization σ^+ with respect to the external magnetic field [7]. However,

in the circumstance in which the magnetic field of the Helmholtz coil majorly eliminates the axial component of the ambient field, subjecting the atomic cell to the remnant transverse component, there now exists a privileged direction for magnetization in the transverse plane [7]. In such a case, the circularly polarized light is orthogonal to the axis of quantization and manifests as a coherent mixture of left, right, and parallel polarizations, $\{\sigma^+, \sigma^-, \pi\}$ along the axis of the magnetic field [7]. In the framework of the experiment, with the radiofrequency modulation off and axial component of the ambient field mostly neutralized by the coil, then upon completion of an optical pumping cycle, the atomic magnetic moment initially is aligned with the direction of beam propagation. Nevertheless, due to the residual transverse ambient field, the magnet moment vector immediately experiences a torque that causes it to precess about the transverse field axis at the ground-state Larmor frequency, ω_L (see Figure 15). Such precessional motion only persists within a timescale on the order of the mean lifetime of the atom's magnetic orientation, in which the oriented direction is disrupted by collisional relaxation [7]. However, before the destabilizing process, the transverse magnetization as a result of precession about the Larmor frequency can be constructed as a function of the external magnetic field. If we define the propagation of optical resonance radiation to be in the \hat{z} direction, then the components of the magnetization attributed to the perpendicular ambient field are approximately [7]:

$$\langle M_{\perp x} \rangle \approx \frac{\Gamma^2}{(\omega_L^2 + \Gamma^2)} \quad (30)$$

$$\langle M_{\perp y} \rangle \approx -\frac{\omega_L \Gamma}{(\omega_L^2 + \Gamma^2)} \quad (31)$$

where $\Gamma = 1/\tau$ is the width between magnetic substates. Upon evaluation, we note that the expression for the magnitude of the transverse magnetization ($|\langle M_{\perp} \rangle| = \sqrt{\langle M_{\perp x} \rangle^2 + \langle M_{\perp y} \rangle^2}$) closely resembles the Lorentzian line profile characteristic to a resonance feature observed within our experiment (Figure 14). Therefore, even in the presence of an exceptionally weak perpendicular magnetic field, the atomic magnetic moments continue to interact with the small finite field and still demonstrate signatures of the weak Zeeman effect detectable by virtue of resonant signals. We refer the reader to reference [7] for the full derivation of transverse magnetization using the Hanle effect.

D. Nuclear Spins

We first determine the ratio between the resonance frequencies of ^{85}Rb and ^{87}Rb expressed in terms of their respective nuclear spins by dividing the Breit-Rabi formula

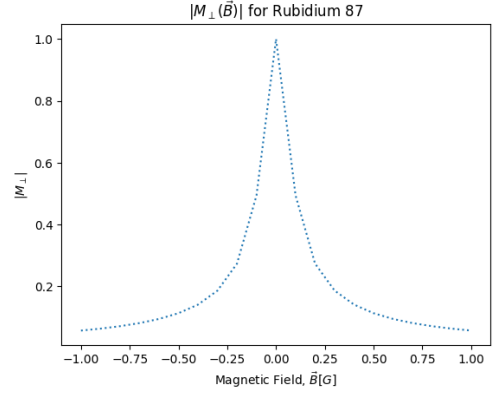


FIG. 14: A very crude simulation for $|\vec{M}_{\perp}(B)|$ for Rubidium 87. To calculate the magnitude, we use the expressions for the components of perpendicular magnetization alongside the Breit-Rabi Equation to construct the transverse magnetization as a function of a weak applied field ranging from [-1,1].

for the two isotopes:

$$\frac{\nu_{85}}{\nu_{87}} = \frac{2I_{87} + 1}{2I_{85} + 1} \quad (32)$$

Plugging in $I_{85} = \frac{5}{2}$ and $I_{87} = \frac{3}{2}$, we can derive the expected ratio,

$$\frac{\nu_{85}}{\nu_{87}} = \frac{2}{3} \quad (33)$$

Further, we contrast the aforementioned value with the resonant frequency data collected from measurement by plotting frequencies for ^{85}Rb against the frequencies for ^{87}Rb and then using linear regression to fit a line to the data, as shown in Figure 16. The best ratio is extracted directly from the slope determined by the regression analysis: $\frac{\nu_{85}}{\nu_{87}} = 0.667 \pm 0.048$. We know that the nuclear spins of both isotopes must be of half-integer form since the number of Zeeman states is a discrete, integer value ($(2F + 1)$). In the linear Zeeman regime for the $5S_{1/2}$ ground state ($J = \frac{1}{2}$),

$$\nu = \frac{|g_F|\mu_B}{h} B, \quad |g_F| = \frac{1}{I + \frac{1}{2}} .$$

Hence, at the same magnetic field,

$$\frac{\nu_{85}}{\nu_{87}} = \frac{|g_F^{(85)}|}{|g_F^{(87)}|} = \frac{\frac{1}{I_{85} + \frac{1}{2}}}{\frac{1}{I_{87} + \frac{1}{2}}} = \frac{I_{87} + \frac{1}{2}}{I_{85} + \frac{1}{2}} .$$

With the fitted ratio $\nu_{85}/\nu_{87} = 0.667 \pm 0.048 \approx 2/3$ and the half-integral constraint, the unique solution is

$$I_{87} = \frac{3}{2}, \quad I_{85} = \frac{5}{2} .$$

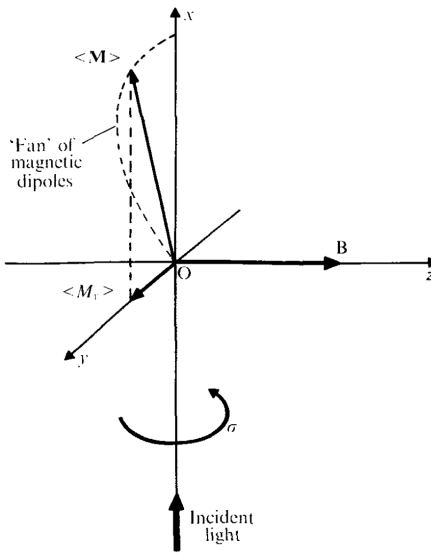


FIG. 15: Transverse optical pumping. The Rubidium atom initially begins in maximum alignment in the \hat{x} direction, however, then precesses in a plane perpendicular to the transverse field applied in \hat{z} . Due to relaxation, the process is gradually damped, but at any point in time, the magnetization will be a culmination of the "fan" of dipole moments precessing at different rates [7]. Figure adapted from ref[7]

Thus, the ratio is sufficient in this $J = \frac{1}{2}$ case; forms like $\nu_{85}/\nu_{87} = \frac{n+1}{k+1}$ do not apply here. We may also use the combination of the Breit-Rabi equation and the resonance vs current plots to facilitate calculation of I_{85} and I_{87} , considering that the slope of the plots are in direct correspondence with the left hand side of the Breit-Rabi equation. Using Equation 13, we convert the current to magnetic field values. Noting that the total field is in fact a combination of the ambient and coil magnetic field, the ambient field value is retrieved using the result from the zero field resonance measurement and serves as an added constant to the converted magnetic field values to derive an estimation of the total external magnetic field imposed on the vapor chamber. We use this particular estimation of the ambient field since it does not require preliminary knowledge of the intrinsic nuclear spins to derive. As such, we again deploy the least squares method to retrieve the optimal slope, $\frac{\nu}{B_{total}}$, and rearrange the Breit-Rabi equation:

$$I = \frac{1}{2}(2.799(\frac{\vec{B}_{total}}{\nu}) - 1) \quad (34)$$

Table VI lists the calculated values for nuclear spin, which are in very close agreement to expected values. Uncertainty bounds associated with the calculated nuclear spins in Table VI are derived via standard error

	I_{85}	I_{87}
Measured	2.54 ± 0.003	1.53 ± 0.0014
Theoretical	2.5	1.5

TABLE VI: Derived vs. Theoretical values for nuclear spin.

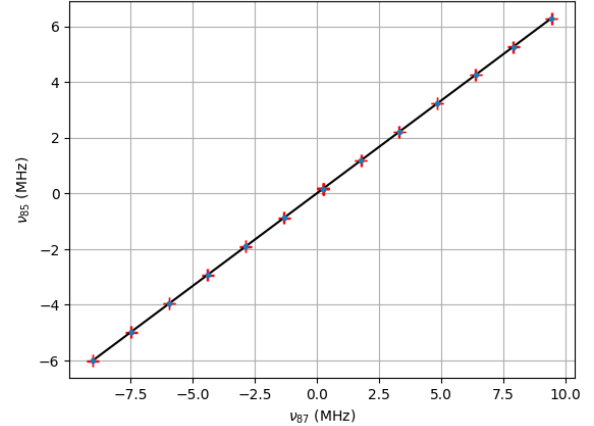


FIG. 16: Plot of the resonant frequencies of Rubidium 87 against the resonant frequencies of Rubidium 85. The errorbars are associated with the systematic errors derived for each frequency.

propagation from the statistical uncertainty associated with the slope $m = \nu/\vec{B}_{total}$:

$$\Delta I = \left| \frac{dI}{dm} \right| \Delta m = \frac{\frac{1}{2}(2.799)}{m^2} \Delta m \quad (35)$$

It is worth remarking that quantification of the nuclear spin values involved the Helmholtz equation to transform our collected current values to the magnetic fields across the coaxial coils. However, this naturally poses as a systematic error, since the actual value for the coil's magnetic field likely does not adhere to ideal Helmholtz conditions - in addition to inhomogeneities, the dimensions of the coil are subject to variation, in which the radii of the turns and the separation between the coils are not precisely unambiguous nor identical. However, we also consider that because the nuclear spins are restricted to take only half-integer values, this potentially renders error analysis as redundant since the results are unequivocal.

1. \vec{B} at the Bulb

Using the nuclear spins derived above, we calculate the magnetic field at the bulb for one positive and negative current value. We choose to use positive current, $i^+ = 1.014$ and negative current, $i^- = -1.014$ to plug into the Breit-Rabi Equation. Error margins for \vec{B} at the bulb using the Helmholtz equation are derived from

the 1% standard uncertainty from the shunt resistor, following Equation 21, whereas bounds for \vec{B} at bulb using the nuclear spins and the Breit Rabi equation were quantified through linear error propagation of both the uncertainties from $\nu(i^\pm)$ and the nuclear spins:

$$\Delta\vec{B} = \sqrt{\left(\frac{\partial\vec{B}}{\partial\nu}\Delta\nu\right)^2 + \left(\frac{\partial\vec{B}}{\partial I}\Delta I\right)^2} \quad (36)$$

Observing the values listed in table VII, we notice a considerable discrepancy between the bulb magnetic field values obtained by the two methods. The difference can be attributed to several factors. Firstly, we omit any contributions from the ambient field when calculating \vec{B}_{bulb} using the Helmholtz equation, and thus the quantities displayed do not account for such external local perturbations. Second, as mentioned in the sections above, the dimensions of the coil are likely not exact, introducing an uncontrollable systematic within our experimental setup.

Current (A)	$\vec{B}_{bulb}(G)$ (Coil)	$\vec{B}_{bulb}(G)$ (I_{85})	$\vec{B}_{bulb}(G)$ (I_{87})
1.014	4.82 ± 0.315	3.863 ± 0.005	3.862 ± 0.004
-1.014	-4.14 ± 0.315	-3.35 ± 0.02	-3.35 ± 0.017

TABLE VII: Calculations for \vec{B}_{bulb}

E. Timescales for Optical Pumping

Following the procedure detailed in Section *Experimental Procedure: Timescales for Optical Pumping*, we provide quantitative estimates for the pumping and relaxation times characteristic to our optical pumping process. As a preliminary estimate, we assess the time spans by studying the time trace on the oscilloscope. We set the oscilloscope to display large divisions of 0.1 sec/div on the horizontal axis and 20mV/div on the vertical axis. Each large division has a granularity of 5 ticks, hence finer-scale divisions for the horizontal and vertical axes were 0.02s/div and 4mV/div, respectively. We define initial conditions at $t = 0$ for pumping time to be the point just prior to exponential ascent towards maximum signal level, such that the system begins in the equilibrium depumped state. From this starting point, we count the discrete, granular divisions on the horizontal axis until the signal reaches $1/e$ of its maximum. Thus, we identify the pumping time to be $\approx 35 - 40$ ms. Conversely, the initial conditions at $t = 0$ for relaxation are identified at the moment just before the signal starts to exponentially decay from its maximum steady level. Then, we again measure the duration over one large scale division and three finer scale intervals, at which the signal has decayed to $1/e$ of its peak amplitude. This yielded a $\approx 160ms$ relaxation time at which point the signal had reached amplitude $\approx 4mV$.

1. Exponential Fit

The following analysis is based on the findings derived in [8]. As an alternative method to deriving pumping and relaxation times, we mark pairs of time and amplitude points across the signal to plot a rough time trace mirroring the display on the oscilloscope and then use an exponential fitting to extract the time constant for optical pumping, τ . The exponential models are derived by considering the rate equations for time dependent population changes in both the highest energy ground state and all other ground states excluding the pumped state. To see this, we isolate our attention to the pumped state of the isotope, ^{87}Rb : $|F = 2, m_F = 2\rangle$. First, we denote $\frac{dn}{dt}$ as the rate of population change in solely the $|F = 2, m_F = 2\rangle$ sublevel and $\frac{dN}{dt}$ as the rate of change in all other states, $|F = 2, m_F \neq 2\rangle$. Then, we designate Rdt as the probability of downward transitions from the pumped state (relaxation) and reciprocally, Pdt as the probability for an upward transition into the pumped state (pumping). Further, we define initial conditions at $t = 0$ to be the point at which the amplified signal amplitude is at an absolute minimum, corresponding to the lowest intensity of transmitted light and greatest opacity of the vapor cell, $I = I_{\min}$. As such, at $t = 0$, we let $n = n_0$ be the initial number of atoms occupying $|F = 2, m_F = 2\rangle$ and $N = N_0$ as initial population in the all other ground state sublevels, and arrive at the rate of change equations for n and N :

$$\frac{dn}{dt} = NPdt - nRdt \quad (37)$$

$$\frac{dN}{dt} = -NPdt + nRdt \quad (38)$$

Solving the differential equations, we obtain:

$$n = n_0 + C_1(1 - e^{-(P+R)t}) \quad (39)$$

$$N = N_0 - C_2(1 - e^{-(P+R)t}) \quad (40)$$

Moreover, we let I_{\max} be the maximum intensity in which the atomic vapor cell has completed an optical pumping cycle and I_{\min} be the minimum intensity in which the atoms are near complete depolarization. Then, making the ground assumption that the intensity of light transmitted through the vapor cell is directly proportional to excess population of atoms in the pumped state, such that

$$I \propto I_{\min} + (n - n_0) \quad (41)$$

we use Equation 39 to derive the transmitted light intensity as a function of time:

$$I = I_{\min} + C(1 - e^{-t/\tau}) \quad (42)$$

yielding the characteristic pumping time $\tau = 1/(P + R)$. In a similar fashion, if we define $t = 0$ as the initial time

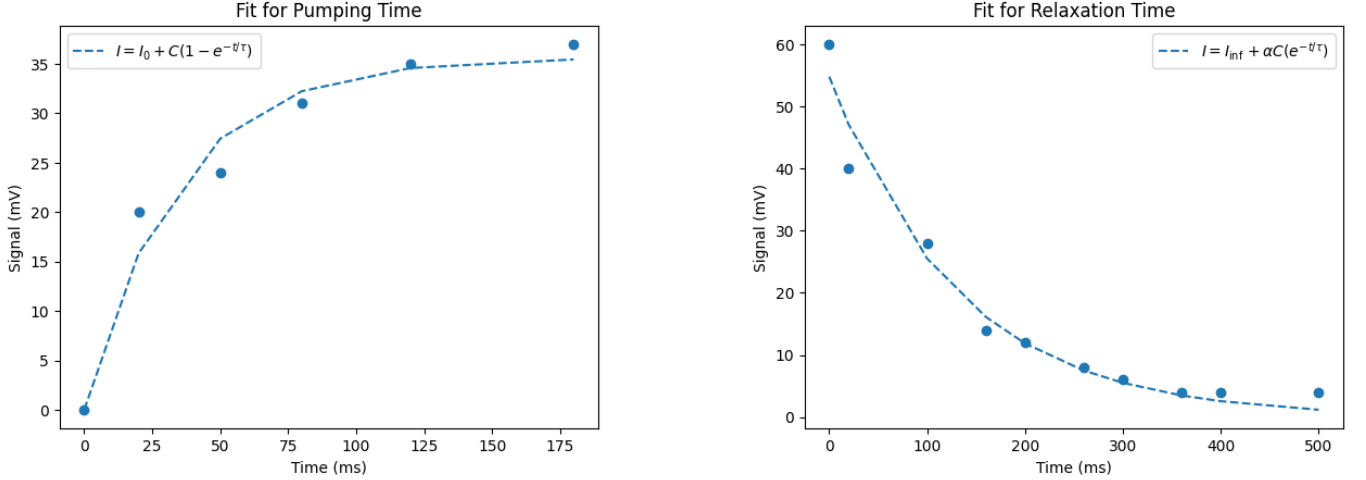


FIG. 17: Extracting time constants from exponential fits to estimate pumping and relaxation times.

in which the atomic system begins in the pumped state such that the transmitted light is I_∞ , then Equation 42 can be written as:

$$I = I_{\max} - Ce^{-t/\tau} \quad (43)$$

As such, we can fit the time-dependent exponential functions to the data points gathered for times and corresponding amplitudes, to extract the characteristic pumping and relaxation times (see Figure 17). Extracting optimal parameters, we derive $\tau_P = 25.97 \pm 2.97\text{ms}$ and $\tau_R = 130.85 \pm 12.67$ for the pumping and relaxation times respectively, which is virtually in alignment with the observed values assessed initially.

F. A Note on Error

To summarize the points of ambiguity with our error estimates, we remark:

1. Every calculation using solely the systematic error derived for ν are inherently underestimated.
2. Every calculation using the Helmholtz equation possesses uncertainty due to magnetic field inhomogeneities and variations in dimensions that cause deviations from ideal Helmholtz configuration of the coils.
3. We omit the 1% error margins from the best-line fits for resonance vs current plots, lending to a one-dimensional biased weights.

V. CONCLUSION

In this work, we investigate the atomic structure of two Rubidium isotopes, ^{85}Rb and ^{87}Rb , under the conditions of a weak, external magnetic field. By sending in

circularly polarized optical photons, we effectively allow complete population in the highest energy ground state. Optically detected magnetic resonance is then achieved by bombarding the vapor cell with near resonant radiofrequency photons to drive transitions between magnetic substates. Such population changes are appraised by optical density measurements in which the population of the isotopes at any instant is inferred by measuring the intensity of the transmitted light. Using these methods, we are able to quantitatively assess resonant signals of each isotope across various values of current and observe the linearity between energy spacings and magnetic field strength, a purely quantum mechanical phenomena induced by the weak Zeeman effect. From the collected data, we calculate nuclear spin values $I_{85} = 2.54 \pm 0.003$ and $I_{87} = 1.53 \pm 0.0014$, falling in close alignment with expected values. We explore several methods to leverage the magnetometry abilities of the Rubidium atoms and derive an estimate for the ambient field in our surroundings. Additionally, by using time domain measurements, we calculate the characteristic pumping and relaxation times for the optical pumping process.

VI. APPENDIX

A. σ^+ Selection Rules

Consider left circularly polarized light delineated by the standard electromagnetic wave equation:

$$E(z, t) = (\hat{x} + i\hat{y})E_0e^{i(kz - \omega t)} \quad (44)$$

in which we define the basis $|L\rangle = \begin{pmatrix} 1 \\ i \end{pmatrix}$. To derive selection rules, we can calculate the expected value

$\langle \psi_f | x + iy | \psi_i \rangle$ using $Y_1^1 \propto \sin \theta e^{i\phi} \propto \frac{x+iy}{r}$:

$$\langle m'l' | x + iy | ml \rangle = \int \int (Y_{l'}^{*m'}(\theta, \phi)) Y_1^1(\theta, \phi) Y_l^m(\theta, \phi) \sin \theta d\theta d\phi \quad (45)$$

in which case, $e^{-im'\phi} e^{i\phi} e^{im\phi} = e^{i(m-m'-1)\phi} \rightarrow m' = m+1$. Upon inspection, it is evident, by virtue of orthogonality of the spherical harmonics, that selection rules for left circularly polarized light must heed $l' = l \pm 1$ and $m' = m+1$ in order to yield a non-null value.

B. Breit-Rabi Derivation

We may again consider Equation 4:

$$H_{hfs} = -\mu_I \cdot (B_J + B) - \mu_J \cdot B \quad (46)$$

$$H_{hfs} = hA\vec{I} \cdot \vec{J} - (\mu_I + \mu_J) \cdot \vec{B} \quad (47)$$

$$H_{hfs} = hA\vec{I} \cdot \vec{J} - \mu_B(g_I\vec{I} + g_J\vec{J}) \cdot \vec{B} \quad (48)$$

Upon observation of Equation (45), we see that the Hamiltonian is governed by the total atomic angular momentum, $\vec{F} = \vec{J} + \vec{I}$. We denote g_F to be the Lande g-factor that relates the different components of the magnetic moments associated with the coupled angular momenta involved in F , as to reveal a net magnetic moment [1]:

$$g_F = g_J \frac{F(F+1) + J(J+1) - I(I+1)}{2F(F+1)} + g_I \frac{F(F+1) - J(J+1) + I(I+1)}{2F(F+1)} \quad (49)$$

(for the sake of brevity, we omit the derivation of the Lande g-factor associated \vec{F}).

With this aside, we can now begin to address each regime of Zeeman effects. First, in the weak field approximation ($\Delta E_Z \ll \Delta E_{hfs}$), the Zeeman splitting is treated as a perturbation to the hyperfine structure Hamiltonian defined in the basis, $|F, m_F\rangle$. In the reciprocal case, for the strong field approximation ($\Delta E_Z \gg \Delta E_{hfs}$), the external magnetic field is so dominating that it effectively decouples spin orbit interactions between \vec{I} and \vec{L} , hence the good basis instead transforms into $|m_I, m_J\rangle$. In either of these cases, the magnetic field splitting is linear with respect to \vec{B} . To address the intermediate magnetic field ($\Delta E_Z \sim \Delta E_{hfs}$),

we enter a regime that mixes the hyperfine sublevels ($|m_I, m_J\rangle$) with the eigenstates of the weak field approximation ($|F, m_F\rangle$). We derive solutions to the Hamiltonian by leveraging total angular momentum conservation, in which case, the magnetic quantum number, m_F , must be equal to the sum of $m_I + m_J$. Moreover, if we define $J = 1/2$, then m_J is restricted to values $\{-\frac{1}{2}, \frac{1}{2}\}$. This subsequently necessitates, $m_F = m_I = \mp 1/2$, and allows us to find our good basis defined by virtue of ladder operators:

$$a_+ |a, a_z\rangle = \sqrt{(a-a_z)(a+a_z+1)} |a, a_z+1\rangle \quad (50)$$

$$a_- |a, a_z\rangle = \sqrt{(a+a_z)(a-a_z+1)} |a, a_z-1\rangle \quad (51)$$

In our scenario,

$$|\pm\rangle = |m_J \pm 1/2, m_F = m_I \mp 1/2\rangle \quad (52)$$

As such, we express the Hamiltonian in Equation (45) in terms of ladder operators for total electronic angular momentum and nuclear spin angular momentum (J_\pm, I_\pm):

$$H = hAI_zJ_z + \frac{hA}{2}(J_+I_- + J_-I_+) - \mu_B B(g_JJ_z + g_IJ_z) \quad (53)$$

By deriving the matrix elements $\langle \pm | H | \pm \rangle$ and $\langle \pm | H | \mp \rangle$, then diagonalizing the matrix to extract eigenvalues, we can determine ΔE in the case $J = 1/2$ ($\Delta F = 1 \pm 1/2$)

$$\Delta E = -\frac{h\Delta W}{2(2I+1)} + \mu_B g_I m_F B \pm \frac{h\Delta W}{2} \sqrt{1 + \frac{2m_F x}{I + \frac{1}{2}} + x^2} \quad (54)$$

$$x \equiv \frac{\mu_B(g_J - g_I)}{h\Delta W} \quad (55)$$

$$\Delta W = A \left(I + \frac{1}{2} \right) \quad (56)$$

Hence, this concludes the full analysis on the intermediate regime.

[1] OPT - Optical Pumping Lab Manual, Physics 111B: Advanced Experimentation Laboratory, University of California, Berkeley.

[2] Optimal Pumping Lab Manual

[3] Optical Pumping of Rubidium, Department of Physics: Indiana University Bloomington

- [4] Steck A. D. Rubidium 85 D Line Data, Oregon Center for Optics and Department of Physics, University of Oregon
- [5] Drullinger, R. E., and R. N. Zare. "Optical pumping of molecules." *The Journal of Chemical Physics*, vol. 51, no. 12, 15 Dec. 1969, pp. 5532–5542
- [6] R.L. De Zafra, "Optical Pumping", *Amer. Journ. of Phys.* 28, 646 (1960)
- [7] Moruzzi, Giovanni. "The Hanle effect and level-crossing spectroscopy—an introduction." *The Hanle Effect and Level-Crossing Spectroscopy*, 1991, pp. 1–46
- [8] Benumof, Reuben. "Optical pumping theory and experiments." *American Journal of Physics*, vol. 33, no. 2, 1 Feb. 1965, pp. 151–160
- [10] Detailed description of an optical pumping experiment "Electron Spin Resonance by Optical Pumping."
- [11] Arimondo, E., et al. "Experimental determinations of the hyperfine structure in the alkali atoms", *Reviews of Modern Physics* 49, 31 (1977)